Vertical Mixing Can Both Induce and Inhibit Submesoscale Frontogenesis

Daniel Patrick Dauhajre[1], Kaushik Srinivasan[1], M Jeroen Molemaker[1], Jonathan Gula[2,3], Delphine Hypolite[1], James C Mcwilliams[1], Roy Barkan[1,4], and William R Young[5]

[1]University of California, Los Angeles
[2]Institut Universitaire de France (IUF)
[3]Univ. Brest, CNRS, Ifremer, IRD, INRIA, Laboratoire d'Oc eanographie Physique et Spatiale
[4]Department of Geosciences, Tel Aviv University
[5]Scripps Institution of Oceanography, University of California

August 08, 2024

Abstract

Past studies separately demonstrate that vertical boundary layer turbulence can either sharpen or weaken submesoscale fronts in the surface mixed layer. These studies invoke competing interpretations that separately focus on the impact of either vertical momentum mixing or vertical buoyancy mixing, where the former can favor sharpening (frontogenesis) by generation of an ageostrophic secondary circulation, while the latter can weaken the front (frontolysis) via diffusion or shear dispersion. No study comprehensively demonstrates vertical mixing induced frontogenesis and frontolysis in a common framework. Here, we develop a unified paradigm for this problem with idealized simulations that explore how a front initially in geostrophic balance responds to a fixed vertical mixing profile. We evolve 2D fronts with the hydrostatic, primitive equations over a range of Ekman (*Ek = 10ˆ{-4} - 10ˆ{-1}*) and Rossby numbers (*Ro = 0.25 - 2*), where *Ek* quantifies the magnitude of vertical mixing and Ro quantifies the initial frontal strength. We observe vertical *momentum* mixing induced, nonlinear frontogenesis at large *Ro* and small *Ek* and inhibition of frontogenesis via vertical *buoyancy* diffusion at small *Ro* and large *Ek* . Symmetric instability can dominate frontogenesis at very small *Ek*; however, the fixed mixing limits interpretation of this regime. Simulations that suppress vertical buoyancy mixing are remarkably frontogenetic, even at large *Ek*, explicitly demonstrating that buoyancy mixing is frontolytic. We identify a controlling parameter (*Roˆ2 / Ek*) that quantifies the competition between cross-front buoyancy advection and vertical diffusion. This parameter approximately maps the transition from frontolysis to frontogenesis across simulations with active buoyancy and momentum mixing.

Vertical Mixing Can Both Induce and Inhibit Submesoscale Frontogenesis

Daniel P. Dauhajre,[a] Kaushik Srinivasan,[a] M. Jeroen Molemaker, [a]
Jonathan Gula,[b,c] Delphine Hypolite,[a] James C. McWilliams,[a] Roy Barkan, [a,d]
William R. Young [e]

[a] *Department of Atmospheric and Oceanic Sciences, University of California Los Angeles*
[b] *Univ. Brest, CNRS, Ifremer, IRD, INRIA, Laboratoire d'Océanographie Physique et Spatiale (LOPS), IUEM, F29280, Plouzané, France*
[c] *Institut Universitaire de France (IUF), Paris, France*
[d] *Department of Geosciences, Tel Aviv University*
[e] *Scripps Institution of Oceanography, University of California, San Diego*

Corresponding author: Daniel P. Dauhajre ddauhajre@atmos.ucla.edu

ABSTRACT: Past studies separately demonstrate that vertical boundary layer turbulence can either sharpen or weaken submesoscale fronts in the surface mixed layer. These studies invoke competing interpretations that separately focus on the impact of either vertical momentum mixing or vertical buoyancy mixing, where the former can favor sharpening (frontogenesis) by generation of an ageostrophic secondary circulation, while the latter can weaken the front (frontolysis) via diffusion or shear dispersion. No study comprehensively demonstrates vertical mixing induced frontogenesis and frontolysis in a common framework. Here, we develop a unified paradigm for this problem with idealized simulations that explore how a front initially in geostrophic balance responds to a fixed vertical mixing profile. We evolve 2D fronts with the hydrostatic, primitive equations over a range of Ekman ($Ek = 10^{-4} - 10^{-1}$) and Rossby numbers ($Ro = 0.25 - 2$), where Ek quantifies the magnitude of vertical mixing and Ro quantifies the initial frontal strength. We observe vertical *momentum* mixing induced, nonlinear frontogenesis at large Ro and small Ek and inhibition of frontogenesis via vertical *buoyancy* diffusion at small Ro and large Ek. Symmetric instability can dominate frontogenesis at very small Ek; however, the fixed mixing limits interpretation of this regime. Simulations that suppress vertical buoyancy mixing are remarkably frontogenetic, even at large Ek, explicitly demonstrating that buoyancy mixing is frontolytic. We identify a controlling parameter $\left(Ro^2/Ek\right)$ that quantifies the competition between cross-front buoyancy advection and vertical diffusion. This parameter approximately maps the transition from frontolysis to frontogenesis across simulations with active buoyancy and momentum mixing.

SIGNIFICANCE STATEMENT: This study reconciles competing views on how vertical mixing on 0.01 - 1 m scales controls the sharpening or weakening of upper-ocean fronts characterized by horizontal changes in density and velocity over 10 - 1000 m scales. The sharpening or weakening of fronts on these scales collectively modulates upper-ocean heat content globally via the modulation of frontal circulation that brings heat upwards. Utilizing simulations, we identify a new, measurable parameter that predicts frontal sharpening or weakening via vertical mixing. This new dynamical framework can better inform the necessary parameterization of these fronts in global climate models. However, future work should interrogate the validity of our simplified model, which unrealistically assumes fixed mixing in time, relative to fronts in nature.

1. Introduction

Submesoscale turbulence (Thomas et al. 2008; McWilliams 2016; Gula et al. 2022; Taylor and Thompson 2023) spawns flow patterns with horizontal scales $O(0.01 - 1\ \mathrm{km})$ and vertical scales $O(1 - 100\ \mathrm{m})$ that frequently populate the surface mixed layer. These submesoscale flow patterns encompass mixed layer eddies (Boccaletti et al. 2007) generated by a form of baroclinic instability and density fronts and filaments (McWilliams 2016). This idealized modeling study focuses on submesoscale fronts, which characteristically exhibit strong, dynamically consequential ageostrophic overturning circulations. These ageostrophic overturning circulations can be triggered and fueled by straining currents – supplied for example, by mixed layer or mesoscale eddies (Zhang et al. 2021) – and/or vertical boundary layer turbulence (Gula et al. 2014; McWilliams et al. 2015; Dauhajre and McWilliams 2018; Barkan et al. 2019). Once activated, an overturning circulation can rapidly sharpen a submesoscale front via amplification of horizontal density and velocity gradients in a process known as frontogenesis (Hoskins 1982; McWilliams 2021). Submesoscale fronts undergoing frontogenesis re-stratify the mixed layer (Taylor and Thompson 2023) while simultaneously serving as conduits for a forward energy cascade (Srinivasan et al. 2023). The conditions required for submesoscale frontogenesis – available potential energy in a surface mixed layer with vertical boundary layer turbulence and/or ambient straining or deformation currents – typically arise in both the open-ocean and continental shelves, making this seemingly spontaneous process pervasive and significant.

Like many other types of oceanic fronts (*e.g.,* gravity fronts), submesoscale fronts exhibit a Rossby number ($Ro = V/fl$) that is $O(1-10)$, often quantified by a horizontal velocity gradient (V/l) normalized by the Coriolis frequency (f). However, unlike other types of fronts, submesoscale fronts (and filaments) uniquely exhibit geostrophic and ageostrophic velocities of comparable of magnitude (Barkan et al. 2019). The horizontal gradients of these velocities result in distinct surface signatures of large cyclonic relative vorticity ($\zeta/f >> 1$; where $\zeta = v_x - u_y$) and convergence ($\delta/f << 1$; where $\delta = u_x + v_y$). The cyclonic vorticity is related to an along-front jet ($\zeta \approx v_x$, where x is the across-front direction) and the convergence indicative of a preferentially downwelling, ageostrophic cross-frontal circulation ($\delta \approx u_x$), commonly referred to as an ageostrophic secondary circulation (ASC). ASCs exhibit extreme vertical velocity ($w \lessapprox -100$ m/day), relative to larger scale currents (Farrar et al. 2020; Taylor and Thompson 2023) and can regulate a variety of oceanic processes, including: energetic exchanges (Molemaker et al. 2010; Su et al. 2018; Srinivasan et al. 2023), smaller-scale turbulence (Buckingham et al. 2019; Wenegrat et al. 2020; Peng et al. 2021; Chor et al. 2022), larger-scale stratification (Fox-Kemper et al. 2011; Su et al. 2018), biogeochemical cycling (Taylor 2016; Freilich et al. 2022; Damien et al. 2023), ecosystem functioning (Levy et al. 2012; Lévy et al. 2018; Fahlbusch et al. 2024), and pollution dispersal (D'Asaro et al. 2018).

Central to understanding the manner in which submesoscale fronts modulate these processes – and fundamental to designing parameterization of submesoscale material fluxes (Young 1994; Fox-Kemper et al. 2008; Zhang et al. 2023; Bodner et al. 2023; Yang et al. 2024) – are the dynamical frameworks that explain how the ASC, and thus the front, strengthens or weakens over a frontal life-cycle, which typically spans hours-to-days and can be externally influenced by other currents or atmospheric forcing. This life-cycle generically encompasses the triggering of a surface convergent ASC that initiates frontogenesis, followed by the subsequent erosion of horizontal density and velocity gradients (frontolysis) by some arresting mechanism (*e.g.,* instability).

This study re-litigates the role of vertical boundary layer turbulence in submesoscale frontogenesis and frontolysis, motivated by competing interpretations (overviewed in Sec. 1a) of whether and how vertical mixing sharpens or weakens submesoscale fronts. Here, vertical boundary layer turbulence refers generally to motions smaller than the submesoscale that drive vertical mixing, which is often represented as a vertical eddy viscosity (ν_v) and diffusivity (κ_v), and considered to be driven by atmospheric forcing or instabilities that can emerge locally at submesoscale fronts (Thomas et al. 2013; Verma et al. 2019; Yu et al. 2019; Carpenter et al. 2020; Peng et al. 2021; Chor et al. 2022). The lack of consensus on this problem stems from dynamical frameworks that separately invoke either the impact of ν_v (in the momentum equation) or κ_v (in the buoyancy equation), where ν_v can setup a convergent ASC that favors frontogenesis (and re-stratifies the mixed layer), while κ_v acts to diffuse the front (and maintains the mixed layer).

While observations shed some light on the coupling between vertical mixing and submesoscale fronts (Nagai et al. 2006; Johnston et al. 2011; Johnson et al. 2020a,b; Carpenter et al. 2020; Swart et al. 2020; Peng et al. 2021), the difficulty in simultaneously measuring spontaneously arising submesoscale fronts as well as smaller-scale turbulence over a range of conditions has left the bulk of mechanistic interpretation to theoretical and numerical treatments. These studies comprise analyses of submesoscale fronts and filaments in realistically configured, primitive equation simulations (Gula et al. 2014; Dauhajre et al. 2017; Wang et al. 2021; Barkan et al. 2019; Srinivasan et al. 2023) as well as more idealized or theoretical approaches that span for example, large-eddy simulations (Sullivan and McWilliams 2017; Crowe and Taylor 2019; Verma et al. 2019; Sullivan and McWilliams 2024), 2D semi-geostrophic (Thompson 2000) or primitive equation (McWilliams et al. 2015) models, asymptotic expansions (Crowe and Taylor 2018; Young 1994), and perturbation analysis (Bodner et al. 2019).

A general approach that isolates the role of vertical mixing evolves an initial front (or filament) that is forced only by vertical mixing, which can be prescribed (Thompson 2000; Crowe and Taylor 2018, 2019; McWilliams 2017), parameterized (McWilliams et al. 2015) or partially resolved (Sullivan and McWilliams 2017; Verma et al. 2019; Sullivan and McWilliams 2024). The two primary controlling parameters inherent in this posing are the initial frontal strength, which can be quantified with a Rossby number ($Ro = \zeta/f, \delta/f$) and the vertical mixing intensity, which can be quantified with an Ekman number ($Ek = \nu_v/fh_{ml}^2$, where h_{ml} is a mixed or turbulent boundary layer depth).

Past studies – many of which employ the above-described approach – separately demonstrate that vertical mixing can either sharpen (Thompson 2000; McWilliams et al. 2015; McWilliams 2017; Sullivan and McWilliams 2017, 2024) or weaken (Young 1994; Crowe and Taylor 2018, 2019; Bodner et al. 2019) fronts. However, these studies sample separate regions of the relevant parameter space (Ek,Ro) (see Table A1), with no individual study demonstrating both vertical mixing induced frontogenesis and frontolysis (for $Ro > 1$) in a common framework. This has led to seemingly disconnected, competing interpretations for the impact of vertical mixing on submesoscale fronts. Below, we heuristically describe these competing views to motivate our attempt to develop a common paradigm for this problem.

a. Competing interpretations on the role of vertical mixing

It is important to first note that, regardless of the role of vertical mixing, frontogenesis is a nonlinear process involving cross-front advection of buoyancy and/or momentum. Barkan et al. (2019) demonstrate that once the ASC Rossby number ($Ro = \delta/f$) reaches $O(1)$, the convergence becomes the primary determinant of frontal sharpening. That is, the question of how vertical mixing impacts frontogenesis primarily concerns whether or not vertical mixing *induces* or *inhibits* the transition to this nonlinear frontogenetic stage.

The prevailing paradigm predicts that vertical mixing induces submesoscale frontogenesis. This view stems from considering the impact of vertical momentum mixing (via ν_v) on thermal wind balance, which results in a linear, three-way balance between rotation, pressure gradient, and vertical momentum mixing. This diagnostic balance dates back to Heaps (1972) and in recent literature is referred to as"turbulent thermal wind (TTW) balance" (Gula et al. 2014; McWilliams et al. 2015; Bachman and Taylor 2016; Crowe and Taylor 2018; Lentz 2022), with Garrett and Loder (1981) providing original theoretical treatment for $Ro < 1$. TTW balance is also contained within the (more generalized) subinertial mixed layer model of Young (1994); it arises as the dominant balance there with 'fast' vertical mixing.

TTW often successfully predicts a surface convergent, frontogenetically favorable ASC for submesoscale fronts and filaments with characteristic $Ro > 1$ in realistic settings (Gula et al. 2014; Dauhajre et al. 2017; Wang et al. 2021; Barkan et al. 2019). A commonly invoked TTW scaling – which assumes only the geostrophic velocity is vertically mixed as in Garrett and Loder (1981) – anticipates stronger convergence for larger ν_v, given the same horizontal density gradient and f (McWilliams 2017). Thus, TTW balance provides a route for vertical *momentum* mixing to setup a convergent, high Ro ASC that can initiate a transition to nonlinear frontogenesis (Barkan et al. 2019), with a prevailing expectation that larger ν_v (and Ek) induces a stronger ASC (larger

$Ro \approx \delta/f$). Interestingly, Barkan et al. (2019) show that the TTW balance describes the 'early-time' (less than one inertial period) convergence of the submesoscale fronts in a realistic submesoscale resolving ocean model solution, which naturally contains straining induced by background mesoscale and mixed-layer eddies.

The framework of 'TTW frontogenesis' often assumes (at least heuristically) that the effect of vertical *buoyancy* mixing is negligible due to weak stratification in the mixed layer (*i.e.*, $\kappa_v \partial b/\partial z \sim 0$, where b is the buoyancy). This heuristic leads to the (unrealistic) prediction that an 'approximately' balanced TTW secondary circulation can sharpen a front until a singularity is reached (see Sec. 6 of McWilliams et al. (2015)). Of course, the weak stratification in the mixed layer is fundamentally due to strong vertical *buoyancy* mixing. More specifically, considering the kinematics of vertical buoyancy mixing acting on a front leads to a perhaps more intuitive, although less invoked, expectation that vertical mixing will weaken a front. This frontolytic view (Young 1994; Crowe and Taylor 2018, 2019) implicates κ_v in weakening fronts via vertical diffusion (at large κ_v, Ek) or shear dispersion (at intermediate κ_v, Ek) (Crowe and Taylor 2018), where oscillations of the vertically sheared ASC coupled to vertical diffusion lead to an effective horizontal diffusivity that spreads isopycnals apart (Young and Jones 1991; Young 1994; Wenegrat et al. 2020; Swart et al. 2020). The asymptotic theory (Crowe and Taylor 2018) underpinning this view can be considered a specialized 2D demonstration of dynamics in the subinertial mixed-layer model of Young (1994). The asymptotic analysis in Crowe and Taylor (2018) is limited to $Ro < 1$, not typical of submesoscale fronts; although, a numerical test of the theory (Crowe and Taylor 2019) suggests validity at $Ro = 1$. The interpretation is that the momentum balance satisfies a 'quasi-steady' (linear) TTW balance, with the buoyancy evolution (vertical diffusion or shear dispersion) dominating frontal evolution. Importantly, this frontolytic interpretation results from focusing primarily on the long-term ($\gtrapprox 10$ inertial periods) solution behavior.

No past studies (summarized in Table A1) account for all of the above-described mechanisms in a common framework, with these heuristics made more complex by the fact that fronts actually modulate the boundary layer turbulence (Verma et al. 2019; Carpenter et al. 2020; Peng et al. 2021; Sullivan and McWilliams 2024). An additional factor contributing to the present confusion is that separate interpretations generally focus on different time-periods: super-inertial (TTW) frontogenesis versus sub-inertial (vertical diffusion or shear dispersion) frontolysis.

b. This study

Here, we attempt to reconcile competing views on this problem with a comprehensive, idealized exploration of vertical mixing (ν_v, κ_v) impacts on submesoscale frontogenesis. By design, we do not consider the impact of straining, which is well-understood to induce frontogenesis (Hoskins and Bretherton 1972; Shakespeare and Taylor 2013); we note that Bodner et al. (2019) find that vertical mixing generally inhibits strain-induced frontogenesis with a perturbation analysis.

Sec. 2 describes the experimental setup, which poses a simple question: how does a surface layer front initially in geostrophic balance evolve in response to the introduction of a prescribed vertical mixing profile ($\nu_v(z), \kappa_v(z)$)? Application of a scaling that assumes comparable along- and across-front velocities at $Ro \sim O(1)$ (Barkan et al. 2019) identifies three controlling non-dimensional parameters: a Rossby number Ro; an Ekman number $Ek = \nu_0 / f h_{ml}^2$, where h_{ml} is a mixed-layer depth, and ν_0 is a mixed-layer average vertical eddy viscosity; and a Prandtl number $Pr = \nu_v / \kappa_v$. This scaling guides the parameter variations in the numerical experiments (Sec. 2c, Table 1) and provides insights into the controlling dynamics. Our idealized setup prescribes an initial front that is motivated by realism (analogous to Sullivan and McWilliams (2017, 2024); Verma et al. (2019); McWilliams et al. (2015)), but explicitly isolates the role of vertical mixing by artificially holding ν_v and κ_v fixed in time (as in Crowe and Taylor (2019)).

The primary numerical experiment evolves 2D fronts over a range of initial frontal strengths ($Ro = 0.25 - 2$) and vertical mixing intensities ($Ek = 10^{-4} - 10^{-1}$) with $Pr = 1$; this is a broader parameter space than previous individual studies. We demonstrate that vertical mixing both induces and inhibits frontogenesis, with all solutions eventually exhibiting frontolysis, and we map these regimes in the (Ek, Ro) space (Sec. 3). Guided by the non-dimensionalized governing equations (Sec. 2b), we demonstrate that the ratio Ro^2/Ek approximately controls the transition from frontogenetic inhibition to frontogenesis (for $Pr = 1$). This mapping of regimes to a single parameter leverages understanding of the distinct roles of ν_v and κ_v in frontogenesis or frontolysis, which is elucidated with simulations that suppress the vertical buoyancy mixing ($\kappa_v = 0, Pr = \infty$). Sec. 4 details the controlling dynamical balances for frontogenetic and frontogenetically inhibited regimes as well as describing the mechanisms controlling late-time frontolysis. Sec. 5 discusses caveats of the idealization and contextualizes our interpretations relative to previous studies and applicability in more realistic environments. Sec. 6 summarizes the results and interpretations of this study.

2. Idealized setup

The basic idealized experiment triggers the evolution of a surface layer density front initially in geostrophic balance with the introduction of a fixed vertical mixing profile $(\nu_v(z), \kappa_v(z))$. We evolve the fronts for a range of vertical mixing intensities (Ek) and initial frontal strengths (Ro) with the hydrostatic, primitive equations in a 2D configuration utilizing the Regional Oceanic Modeling System (ROMS; Shchepetkin and McWilliams (2005)). Here, we define the 2D system (Sec. 2a), identify controlling non-dimensional parameters (Sec. 2b), and detail the ROMS idealized setup and experimental design (Sec. 2c).

a. 2D system

We take the hydrostatic, primitive equations with x, y as the across and along-front directions, respectively. For simplicity, we assume along-front uniformity $\partial/\partial y = 0$ and a vertically variable mixing profile $(\nu_v(z), \kappa_v(z))$. This gives the 2D (x, z) system:

$$D_t u - f v = -\phi_x + \frac{\partial}{\partial z}(\nu_v u_z) \ , \tag{1a}$$

$$D_t v + f u = \frac{\partial}{\partial z}(\nu_v v_z) \ , \tag{1b}$$

$$D_t b = \frac{\partial}{\partial z}(\kappa_v b_z) \ , \tag{1c}$$

$$\phi_z = b \ , \tag{1d}$$

$$u_x + w_z = 0 \ , \tag{1e}$$

where $D_t = \partial_t + u\partial_x + w\partial_z$ is the material derivative, u is the across-front velocity, v is the along-front velocity, $\phi = p/\rho_0$ is the pressure normalized by a reference density ρ_0, and $b = -g\rho/\rho_0$ is the buoyancy.

The horizontal boundary conditions are periodic in x and the vertical boundary conditions are zero buoyancy flux and zero stress at the free-surface $(z = \eta)$ and a zero buoyancy flux and a bottom stress ($\vec{\tau}^b$) at the (flat) bottom ($z = -H$).

$$\nu_\mathrm{v} \frac{\partial \vec{u}_h}{\partial z} = 0, \quad \text{at } z = \eta \tag{2a}$$

$$\nu_\mathrm{v} \frac{\partial \vec{u}_h}{\partial z} = \frac{\vec{\tau}^b}{\rho_0}, \quad \text{at } z = -H \tag{2b}$$

$$\kappa_\mathrm{v} \frac{\partial b}{\partial z} = 0, \quad \text{at } z = \eta, -H \tag{2c}$$

The bottom boundary conditions have little significance on the near-surface behavior that is the focus of this study.

TTW balance (Sec. 1a) is given by removing the D_t terms in Eq. 1a-1b. Including acceleration ($\partial u/\partial t$, $\partial v/\partial t$) in TTW gives the 'transient' TTW (or 'T^{3}W') balance (Dauhajre and McWilliams 2018; Wenegrat and McPhaden 2016), which is discussed in Sec. 4.

b. Nondimensionalization

Scaling Eq. (1) identifies the controlling non-dimensional parameters. We follow the scaling in Barkan et al. (2019), which makes two primary assumptions: (a) comparable along-front (v) and across front velocity (u) for $Ro \sim O(1)$ and (b) anisotropy of SM fronts ($l/L << 1$) in a surface mixed layer of depth h_{ml}, where l and L are across- and along-front length scales, respectively. The 2D system (1) has no along-front dimension, so $l/L << 1$ by construction. The scaling is as follows:

$$x \sim l, \quad z \sim h_{ml} \tag{3a}$$

$$v \sim V, \quad u \sim RoV, \quad w \sim RoV\frac{h_{ml}}{l} \tag{3b}$$

$$t \sim \frac{l}{RoV}, \quad \phi \sim fVl, \quad b \sim \frac{fVl}{h_{ml}} \tag{3c}$$

$$\nu_\mathrm{v} \sim \nu_0, \quad \kappa_\mathrm{v} \sim \kappa_0 \tag{3d}$$

Applying (3) to (1) gives

$$\frac{Ro^2}{Ek}[D_t u] - \frac{1}{RoEk}[v] = -\frac{1}{RoEk}[\phi_x] + [u_{zz}] \ , \tag{4a}$$

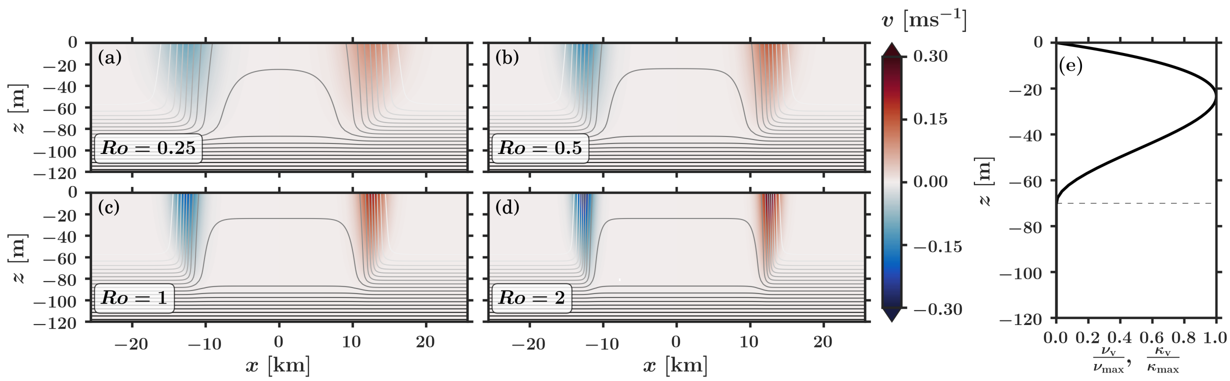

FIG. 1. Idealized 2D (x,z) double front initial conditions (a-d) and prescribed vertical mixing profile (e) normalized by a maximum ($\nu_{\max}$) (a-d): initial temperature (contour lines) and along-front velocity (v, colors). The initial condition is in geostrophic balance and there is no initial across-front velocity ($u(t=0)=0$). The initial Rossby number is defined based on the surface relative vorticity normalized by the the Coriolis frequency ($Ro = v_x/f$). The Ekman number (Ek) is defined based on the vertical average of $\nu_{\mathrm{v}}(z)$ in the mixed layer and is modulated via $\nu_{\max}$. The isotherms in (a-d) are the same in every panel and range from 23.74 ^oC (black lines) to 24.66 ^oC (white lines) with 0.051 ^oC change between each isotherm. Any (x,z) snapshots that follow show the same isotherms as here; the simulations employ a linear equation of state, dependent only on temperature, so these isotherms can be interpreted as isopycnals. All analyses focus on the eastern front ($x > 0$), noting that both fronts behave the same. Appendix B details formulations for the initial condition and vertical mixing profile.

$$\frac{Ro^2}{Ek}[D_t v] + \frac{Ro}{Ek}[u] = [v_{zz}] \ , \tag{4b}$$

$$\frac{Pr\,Ro^2}{Ek}[D_t b] = [b_{zz}] \ , \tag{4c}$$

$$[\phi_z] = [b] \ , \tag{4d}$$

$$[u_x] + [w_z] = 0 \ , \tag{4e}$$

where the brackets denote non-dimensionalized terms. The controlling non-dimensional parameters are the Rossby number ($Ro = V/fl$), the Ekman number $\left(Ek = \nu_0/f h_{ml}^2\right)$, and the Prandtl number ($Pr = \nu_0/\kappa_0$), with ν_0, κ_0 as constants (and can be considered maxima or vertical averages of $\nu_{\mathrm{v}}(z), \kappa_{\mathrm{v}}(z)$). Note that all the nonlinear terms $[D_t u], [D_t v], [D_t b]$ are scaled by Ro^2/Ek, assuming that $Pr = 1$.

TABLE 1. Parameters for sets of idealized simulations. The controlling non-dimensional parameters (Sec. 2b) for each case comprise the Rossby number, based on the geostrophic initial condition ($Ro = \zeta_{init}/f$, where $\zeta = v_x$ at $t = 0$; see Fig. 1a-d); the Ekman number $\left(Ek = \nu_v/(h_{ml}^2 f)\right)$; and the Prandtl number ($Pr = \nu_v/\kappa_v$). We define Ek based on a fixed mixed layer depth $h_{ml} = 70$ m and the mixed layer mean of the prescribed vertical eddy viscosity profile (Fig. 1e) that is constant in the cross-front direction (x) and time. In all cases, $f = 10^{-4}$ s^{-1}. The simulations comprise three solution sets: (1) a primary set of 16 cases (4 Ro numbers × 4 Ek numbers) with $Pr = 1$; (2) a secondary set where vertical buoyancy mixing is suppressed ($\kappa_v = 0$, $Pr = \infty$); and (3) two cases with fixed $Ro^2/Ek (= 350.87)$ corresponding to the $Ro = 2$, $Ek = 1.14 \times 10^{-2}$ case (see Sec. 3c). Movies S1 and S2 illustrate the ASC and density evolution for primary and buoyancy mixing suppression solution sets, respectively. The listed Ek contain a 1.14 multiplicative factor for the first two solution sets that comes from the vertical average of the non-dimensional ν_v profile in Fig. 1e, which is 0.56. This gives $Ek = 0.56\nu_{\max}/f h_{ml}^2 = 1.14\nu_{\max}$; we refer to Ek in the text and subsequent figures without this factor (*e.g.,* $Ek = 10^{-2}$) for brevity.

Solution set	**Number of solutions**	***Ro***	***Ek***	***Pr***
Primary	16	[0.25 0.5, 1, 2]	$1.14 \times [10^{-4}, 10^{-3}, 10^{-2}, 10^{-1}]$	1
Buoyancy mixing suppression	16	[0.25 0.5, 1, 2]	$1.14 \times [10^{-4}, 10^{-3}, 10^{-2}, 10^{-1}]$	∞
Fixed Ro^2/Ek	2	1,4	$2.85 \times 10^{-3}, 4.56 \times 10^{-2}$	1

Assuming a geostrophic initial condition, (with $u(t = 0) = 0; v(t = 0) = \phi_x/f$), $Ek \rightarrow 0$ gives geostrophic balance (middle two terms in Eq. (4a)) and no evolution is expected. For $Pr = 1$, $Ro^2/Ek << 1$, and $Ro << 1$, the nonlinear terms become unimportant and the leading order approximation is linear, characterized by a TTW momentum balance and vertical diffusion dominated buoyancy balance (*i.e.,* analogous to the interpretation of Crowe and Taylor (2018)). However, our dynamical target is $Ro \sim O(1)$, for $Ek < 1$, which is more typical of submesoscale fronts in upper-ocean (for example, see Fig. 2 in the supplementary materials). We anticipate nonlinear contributions to the frontal evolution in this regime and utilize the numerical experiments to map the regime transitions in Ek, Ro.

c. *ROMS experimental design*

We solve Eq. (1) with the UCLA ROMS code, utilizing an idealized, 2D (x, z) configuration (Fig. 1). ROMS solves the primitive equations in a terrain-following coordinate system with an implicitly hyper-diffusive, 3rd-order upstream advection scheme for horizontal advection and a parabolic spline scheme for vertical advection of momenta and tracers. The idealized configuration employs a flat bottom ($H = 500$ m); periodic boundary conditions in the cross-front (x) direction; constant horizontal resolution ($\Delta x = 50$ m) over a domain length of of 51.2 km; 128 vertical levels with grid-stretching parameters $\theta_s = 6$, $\theta_b = 2$, $h_c = 25$; and constant Coriolis frequency $f = 1 \times 10^{-4}$ s^{-1}. The buoyancy is defined as a linear function of temperature with $\rho_0 = 1000$ kg/m^3 and thermal expansion coefficient $\alpha = 2 \times 10^{-4}$. In practice, the 2D configuration is achieved with 4 grid-points in the along-front direction (y), periodic boundary conditions in y, and an initial condition that is uniform in y.

The experimental setup prescribes an initial 2D buoyancy field (Fig. 1a-d) with a geostrophic, along-front velocity (v) and triggers frontal evolution with the introduction of a vertically variable mixing profile $(\nu_v(z), \kappa_v(z))$ that is constant in the cross-front direction and time (Fig. 1e). This idealized setup (Fig. 1) sits between the intended realism of the LES solutions in Sullivan and McWilliams (2017, 2024) – that partially resolve the evolving boundary layer turbulence – and the extreme idealization of Crowe and Taylor (2018, 2019, 2020) that poses the problem with no initial stratification and constant mixing in space and time. The latter studies employ an initial condition that satisfies TTW balance; this modifies both $v(t = 0)$ and introduces a secondary circulation (u, w) at $t = 0$ relative to our geostrophic initial condition. Based on testing a subset of cases with a TTW-balanced initial condition (not shown) we do not expect the choice of initial condition (TTW or geostrophic) to impact the results, as the secondary circulation develops via a transient adjustment with a geostrophic initial condition (detailed in Sec. 4).

The initial condition (Fig. 1a-d) defines a surface mixed layer with a weak stratification $\left(b_z = N^2 \sim 10^{-7}\ \mathrm{s}^{-2}\right)$ and horizontal buoyancy gradient b_x that transitions to a pycnocline and interior stratification $\left(N^2 \sim 10^{-5}\ \mathrm{s}^{-2}\right)$. The surface mixed layer depth $h_{ml}(x)$ varies between 60 m and 75 m over a frontal width that is modulated to set the magnitude of the initial horizontal buoyancy gradient. The prescribed vertical eddy viscosity and diffusivity profile (Fig. 1e) is zero at the surface (to ensure zero-stress), reaches a maxima $(\nu_{\max}, \kappa_{\max})$ in the mixed layer interior, and transitions to zero at $z = -70$ m (an approximate base of the mixed layer). This mixing shape approximately maintains the mixed layer density structure while minimizing entrainment from the pycnocline. To ensure across-front periodicity, the initial condition comprises a double front (Fig.

1a-d). Appendix B details the initial condition and mixing profile formulations. Analyses focus on the front on the eastern end of the domain ($x > 0$), noting that the fronts evolve symmetrically.

We evolve fronts for a range of initial frontal strengths ($\max[b_x(t=0)]$) and vertical mixing intensities (defined based on $\nu_{\max}, \kappa_{\max}$; Fig. 1e). This parameter variation translates to varying the initial Rossby number ($Ro = \max[\zeta_{init}]/f$, where $\zeta_{init} = v_x$ at $t = 0$) and an Ekman number $\left(Ek = \nu_0/f h_{ml}^2\right)$, where ν_0 is the average of $\nu(z)$ in the upper 70 m. We run 34 total simulations (Table 1): two solutions sets of 16 solutions each as well as 2 more simulations with fixed Ro^2/Ek. The primary solution set consists of four $Ro(= 0.25, 0.5, 1, 2$; Fig. 1a-d) by four $Ek = \left(1.14 \times \left[10^{-4}, 10^{-3}, 10^{-2}, 10^{-1}\right]\right)$ [1] with $Pr = \nu_{\mathrm{v}}/\kappa_{\mathrm{v}} = 1$. The second set of solutions suppresses the buoyancy diffusivity ($\kappa_{\mathrm{v}} = 0$, $Pr = \infty$) for the same Ek, Ro as the primary solution set. These solutions allow us to distinguish the roles of ν_{v} and κ_{v} in governing frontal evolution (Sec. 3d; Eq. (4)). The third set of solutions comprises two cases with fixed Ro^2/Ek (see Sec. 2b) corresponding to a case in the primary solution set with $Ro = 2$, $Ek = 1.14 \times 10^{-2}$ ($Ro^2/Ek = 350.87$). These solutions provide an additional test on the utility of Ro^2/Ek as a governing parameter for vertical mixing induced frontogenesis (see Sec. 3c).

All cases are run for ≈ 5 inertial periods ($T_i = 2\pi/f$) with a time-step $\Delta t = 15$ s. Model output (u, v, w, ρ, η) is stored as instantaneous snapshots and saved every 15 minutes. We compute diagnostic terms in the momentum equations online with the model time-step, which we use to describe the controlling balances during frontal evolution (Sec. 4).

The model resolution ($\Delta x = 50$ m) adequately resolves a submesoscale frontal width of $\sim O(100\text{ m})$. However, we note that the initial condition contains very weak mixed layer stratification $\left(N^2 \sim 10^{-7}\text{ s}^{-2}\right)$, strong vertical shear, and negative potential vorticity (Fig. B1). These conditions make some solutions susceptible to symmetric or shear instabilities, with the former dominating solution behavior at $Ek = 10^{-4}$, where the fixed vertical mixing is too weak to suppress these motions. While these instabilities are known to occur at submesoscale fronts with stratification and shear similar to our initial conditions (Yu et al. 2019; Peng et al. 2021), they are incompletely resolved in the present simulations due to the inability of the vertical mixing to respond to their onset, the hydrostatic assumption, and resolution limitations. Sec. 5 discusses these instabilities and their impact on our interpretations.

[1] In subsequent text and figures we generally do not list the 1.14 factor for Ek; see Table 1 caption.

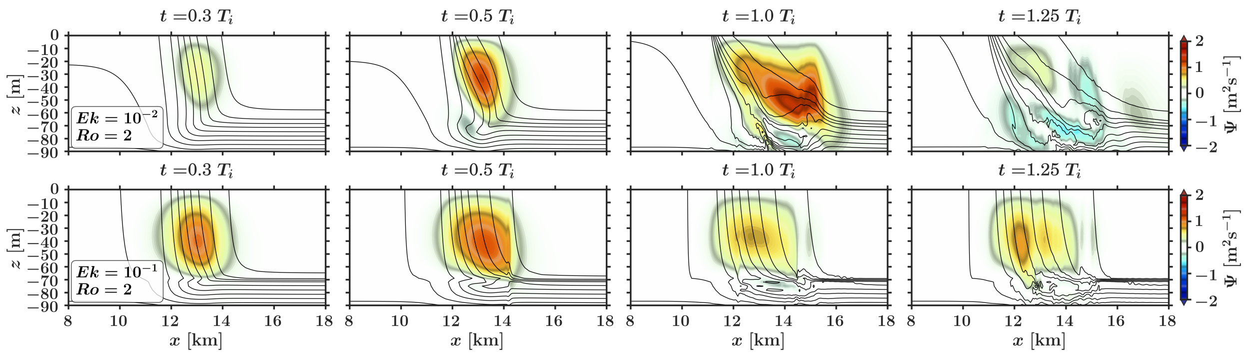

FIG. 2. Snapshots of isopycnals (black lines) and ageostrophic secondary circulation (ASC) streamfunction (colors, $\Psi(x,z)$, where $u = \partial\Psi/\partial z$ and $w = -\partial\Psi/\partial x$) for two cases in the primary solution set ($Pr = 1$; see Table 1); Ek and Ro are indicated in the first snapshot (left column) for each solution. These solutions (both with initial $Ro = 2$, Fig. 1d) demonstrate vertical mixing induced frontogenesis (top; $Ek = 10^{-2}$) and vertical mixing inhibition of frontogenesis (bottom; $Ek = 10^{-1}$). The isopycnal contours for both cases are the same as in Fig. 1. Note the surface-intensified sharpening of the front at $Ek = 10^{-2}$ (top; $t = 1\,T_i$) compared to the stronger mixing case (bottom; $Ek = 10^{-1}$), despite the presence of non-zero ASC ($\Psi > 0$). In both cases, introduction of the vertical momentum mixing (ν_v) induces the generation of the ASC (Sec. 4 details this adjustment).

3. Vertical mixing induces and inhibits frontogenesis

a. Illustrative solutions

Here, we overview the evolution of two solutions (Fig. 2) to illustrate two typical responses to vertical mixing: frontogenesis (Fig. 2 top; $Ek = 10^{-2}$, $Ro = 2$, $Pr = 1$) and frontogenetic inhibition (Fig. 2 bottom; $Ek = 10^{-1}$, $Ro = 2$, $Pr = 1$). The snapshot sequences in Fig. 2 show the evolution of the density (contour lines) and ageostrophic secondary circulation (ASC) streamfunction (colors, $\Psi(x,z)$, where $u = \partial\Psi/\partial z$ and $w = -\partial\Psi/\partial x$). Movie S1 shows the evolution of these fields for all cases in the primary solution set (Table 1).

In both cases in Fig. 2 (with $Ro = 2, Pr = 1$ and differing Ek) an ASC develops, indicating a generic momentum adjustment to the introduction of vertical momentum mixing. The ASC acts counterclockwise ($\Psi > 0$) in the (x,z) plane in a manner that favors re-stratification of the mixed layer (pushing lighter water over heavier water). While both cases exhibit this ASC, the frontal evolution is different. With stronger mixing ($Ek = 10^{-1}$; Fig. 2 bottom), the ASC weakens and there is no discernible frontal sharpening (or spreading). With weaker mixing ($Ek = 10^{-2}$; Fig. 2

top), the front sharpens (over approximately 1 inertial period), with this sharpening characterized by amplification of b_x and Ψ. We characterize the top row of Fig. 2 as frontogenesis and the bottom row of Fig. 2 as frontogenetic inhibition, noting that frontolysis occurs at later time for a majority of the cases with $Pr = 1$ (see weakening of the ASC in Fig. 2 top right, Movie SI, or Fig. 3). Sec. 4 provides more detailed descriptions of the dynamics controlling these characteristic sequences.

b. Solution regimes

Fig. 3 provides a visualization of solution regimes in the (Ek, Ro) space with (x,t) Hovmöller plots of the surface, cross-front buoyancy gradient that is normalized relative to the maximum b_x in the initial condition:

$$\widetilde{b_x} = \frac{b_x(x,t)}{\max[b_x(x,t=0)]} - 1 \ . \tag{5}$$

We observe three regimes in the primary solution set ($Pr = 1$; Fig. 3): 'typical' frontogenesis via the ASC (Fig. 2 top, Fig. 3b,c), frontogenetic inhibition or frontolysis (Fig. 2 bottom, *e.g.,* Fig. 3d,h), and frontogenesis via (incompletely resolved) symmetric instability (Fig. 3i). We define frontogenesis in Fig. 3 as a sustained increase of the (surface) buoyancy gradient over ≈ 1 inertial period. These frontogenetic cases (*e.g.,* Fig. 3b,c) are characterized by a growth and peak in $\widetilde{b_x}$ that generally weakens at later time (*e.g.,* Fig. 3c). This late-time weakening can be due to inertial oscillations that reverse the ASC and weaken b_x (*e.g.,* see $x \approx 12$ km, $t \approx 2\,T_i$ in Fig. 3b). These late-stage inertial oscillations, detailed further in Sec. 4, occur in many of the solutions and are less damped with weaker mixing (see Movie S1).

In all cases the front moves laterally (to the left in Fig. 3), with this movement most pronounced at larger Ro and smaller Ek. Some of the strongly frontogenetic cases also exhibit the formation of a secondary front (*e.g.,* Fig. 3a, $x \gtrapprox 14$ km). However, we do not focus on this behavior, which is likely a byproduct of the fixed vertical mixing.

Fig. 3 illustrates general trends of stronger frontogenesis (darker reds) for decreasing Ek or increasing Ro. In particular, there is a frontogenetic 'sweet spot' (Fig. 3b,c,f,g) at large Ro ($Ro \gtrapprox 1$) and intermediate Ek ($Ek = 10^{-3} - 10^{-2}$). Very strong mixing ($Ek = 10^{-1}$; right column, Fig. 3) or very weak initial fronts ($Ro = 0.25$; bottom row, Fig. 3) exhibit extremely weak or no frontogenesis for $t \leq 3\,T_i$.

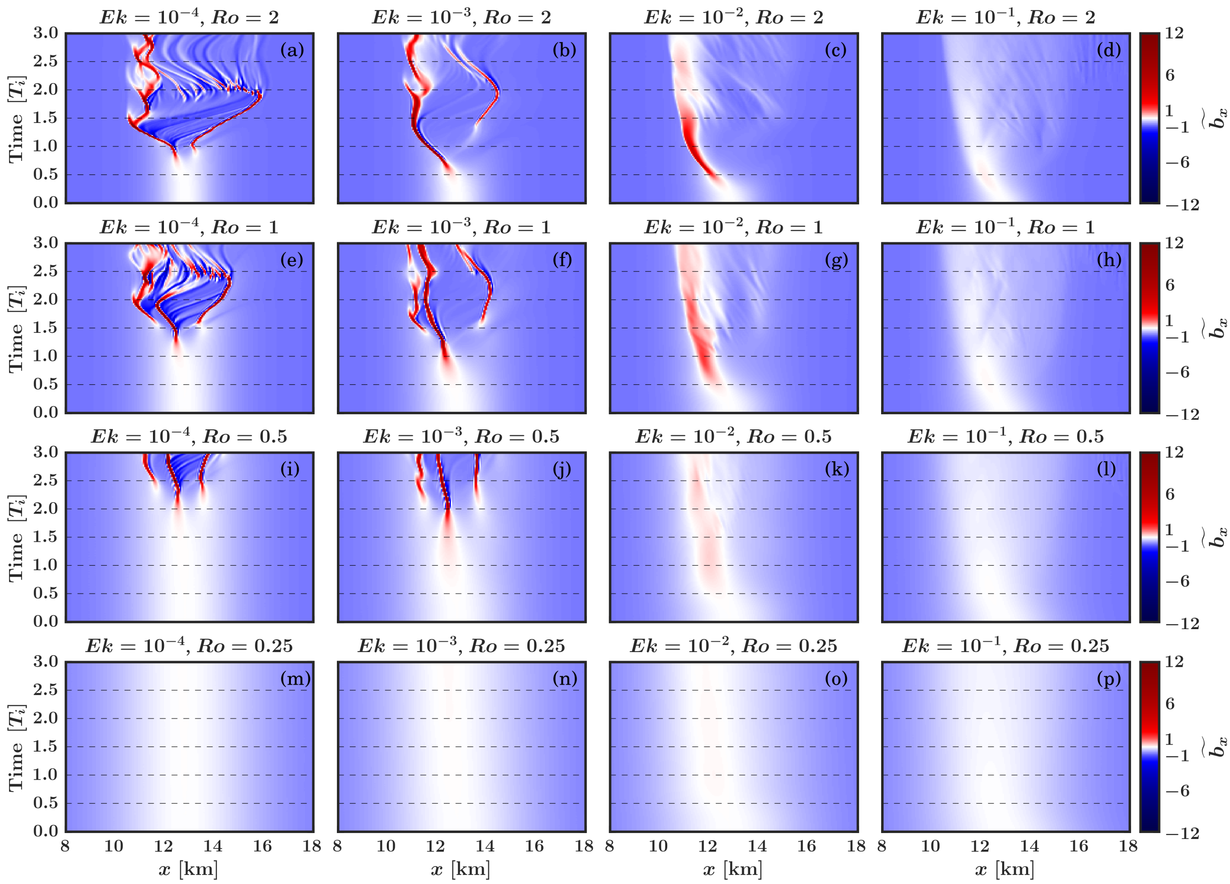

FIG. 3. Vertical mixing induced frontogenesis and frontolysis across Ekman (Ek; columns) and Rossby numbers (Ro; rows) in the primary solution set (Table 1). Each panel shows a (x,t) Hovmöller of the surface cross-front buoyancy gradient that is normalized relative to maximum buoyancy gradient in the initial condition $\left(\widetilde{b_x}\right)$ (Eq. 5); $\widetilde{b_x}$ is dimensionless. All panels share the same colorbar, which is log-scaled for better visualization. The vertical time axis has units of inertial period $T_i = 2\pi/f$. Here, frontogenesis appears as a red 'streak'. Note the stronger frontogenesis at smaller Ek and larger Ro and extremely weak to no frontogenesis at larger Ek and smaller Ro.

The weakest mixing cases ($Ek = 10^{-4}$, Fig. 3) also exhibit strong frontogenesis that takes a distinct three-front structure, particularly for smaller Ro (*e.g.,* Fig. 3i). This frontogenesis is due to the onset of symmetric instability (SI), which occurs most prominently at $Ek = 10^{-4}$ and small Ro, but also appears at $Ek = 10^{-3}$ to varying degrees (*e.g.,* Fig. 3j). We do not over-interpret the low Ek and low Ro solutions dominated by later-time SI (Fig. 3i,j,m,n; where SI appears off-axis

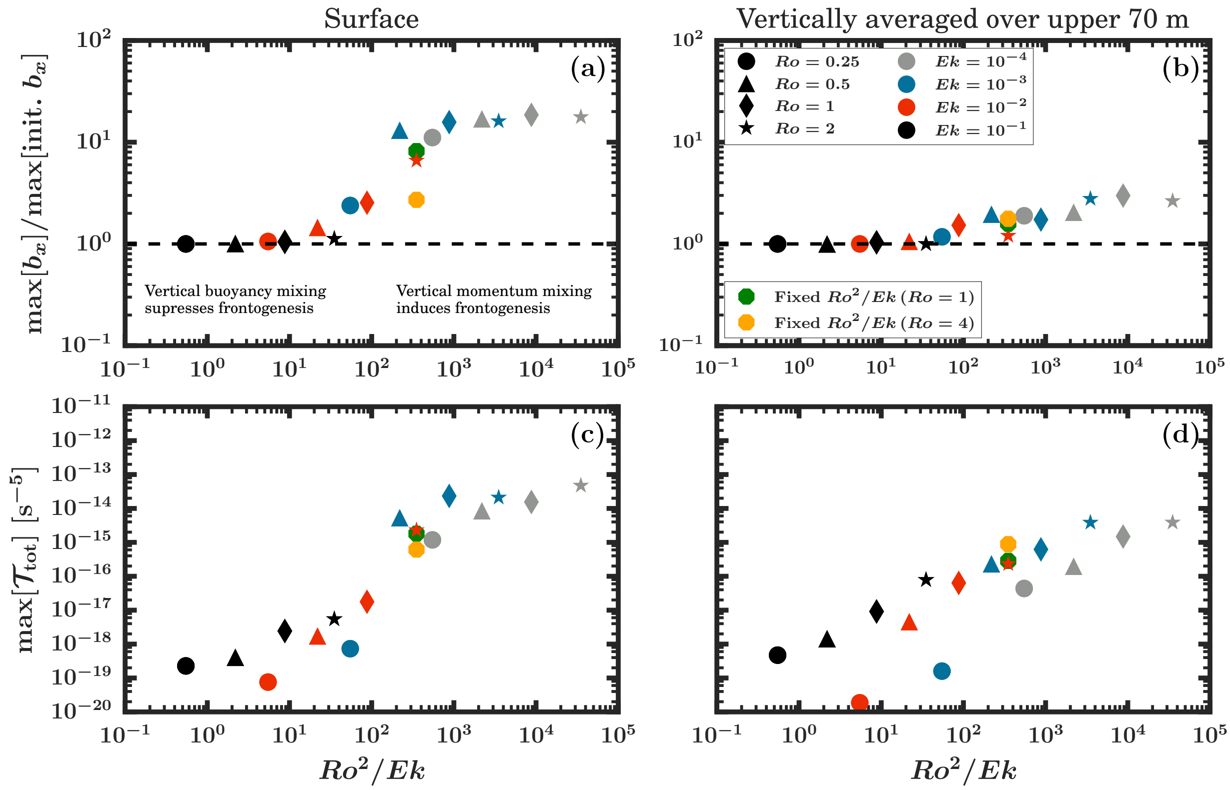

FIG. 4. Surface (left) and vertically averaged (right) metrics of frontogenesis as a function of Ro^2/Ek (see Sec. 2b) for solutions with $Pr = 1$. The top left legend in (b) indicates Ek (color) and Ro (marker shape) for each case in the primary solution set (first row, Table 1). The green and orange octagons represent cases with fixed Ro^2/Ek (corresponding to the red star case; $Ro = 2$ $Ek = 10^{-2}$), but different Ro and Ek (with Ro indicated in the legend, see bottom row Table 1). The top panels (a,b) measure frontogenesis as the ratio of the maximum buoyancy gradient ($\max[b_x]$) normalized by the initial condition ($\max[\text{init. } b_x]$); values greater than 1 (horizontal dashed line) indicate frontal sharpening. The bottom panels (c,d) measure frontogenesis as the maximum buoyancy frontogenetic tendency rate ($\max[\mathcal{T}_{\text{tot}}]$); $\mathcal{T}_{\text{tot}}$ is defined in Eq. (6)). For both frontogenesis metrics, maximum values are taken over the entire simulation period (5.5 inertial periods) with most cases with exhibiting maximum b_x before ≈ 3 inertial periods (see Fig. 3). The inset text in (a) summarizes interpretations, detailed in Sec. 3c. Note that solutions with both low Ek and Ro (*e.g.,* grey circle) exhibit frontogenesis due to symmetric instability (see Sec. 5a) that is distinct from the frontogenesis via an ageostrophic secondary circulation induced by vertical momentum mixing (*e.g.,* red star).

at $t \approx 5\,T_i$ for $Ro = 0.25$ in Fig. 3m,n), primarily due to the fixed vertical mixing assumption that limits their fluid dynamical validity. We discuss these instabilities further in Sec. 5a.

All solutions exhibit a transient response (*i.e.,* non-steady b_x), indicating the breaking of geostrophic balance by the vertical momentum mixing (or onset of SI). In the typical (non-SI) frontogenetic cases (*e.g.,* Fig. 3b,c) the increase in b_x is driven by the convergent ASC (*e.g.,* Fig. 2, top) that develops in response to this balance-breaking. Fig. 3 makes apparent the Ek and Ro dependence on the time-scale over which the ASC and frontogenesis develop. As Ek or Ro increase, the initiation of frontogenesis (red streaks in Fig. 3) occurs earlier. However, larger Ek also results in faster and stronger erosion of the front (*e.g.,* late-time presence or absence of dark red moving from left to right in the top row of Fig. 3). This suggests an intrinsic competition between the frontogenetic ASC – triggered (faster) by (stronger) vertical *momentum* mixing – and the vertically diffusive erosion of the front triggered (faster) by (stronger) vertical *buoyancy* mixing.

c. Controlling parameter: Ro^2/Ek

Frontogenesis involves nonlinear advection in the momentum and/or buoyancy equation. The scaled primitive equation system (Eq. (4)) suggests that Ro^2/Ek sets the importance of these nonlinear terms in both the momentum and buoyancy equations. If we assume that a primary function of the momentum equation is to trigger the ASC (detailed in Sec. 4), we can assume that the buoyancy equation (Eq. 4c) controls the outcome (frontal sharpening or weakening). That is, horizontal buoyancy advection $\left(Ro^2 Pr[ub_x]\right)$ competes against vertical diffusion $(Ek[b_{zz}])$ (see Eq. 4c). Taking $Pr = 1$, this implies a fundamental control on frontal evolution by Ro^2/Ek; this competition is also highlighted in Thompson (2000), albeit with a different scaling and for a semi-geostrophic system.

Fig. 4 demonstrates that Ro^2/Ek approximately maps the transition between frontogenetically inhibited or frontolytic $\left(Ro^2/Ek < 50\right)$ and frontogenetic $(Ro^2/Ek \gtrsim 50)$ solutions for two metrics of frontogenesis: the maximum buoyancy gradient normalized by the initial condition maxima ($\max[b_x]/\max[\text{init. } b_x]$; Fig. 4a,b) or the maximum buoyancy frontogenetic tendency rate ($\max[\mathcal{T}_{\text{tot}}]$; Fig. 4c,d), where $\mathcal{T}_{\text{tot}}$ represents the change of amplitude of the buoyancy gradient following a fluid parcel (*i.e.,* the rate of frontal sharpening; see Eq. (6) for a complete definition). These metrics are defined relative to the maximum taken over all time. The surface metrics of frontogenesis (Fig. 4a,c) most successfully map regime transitions. The mixed layer average metrics

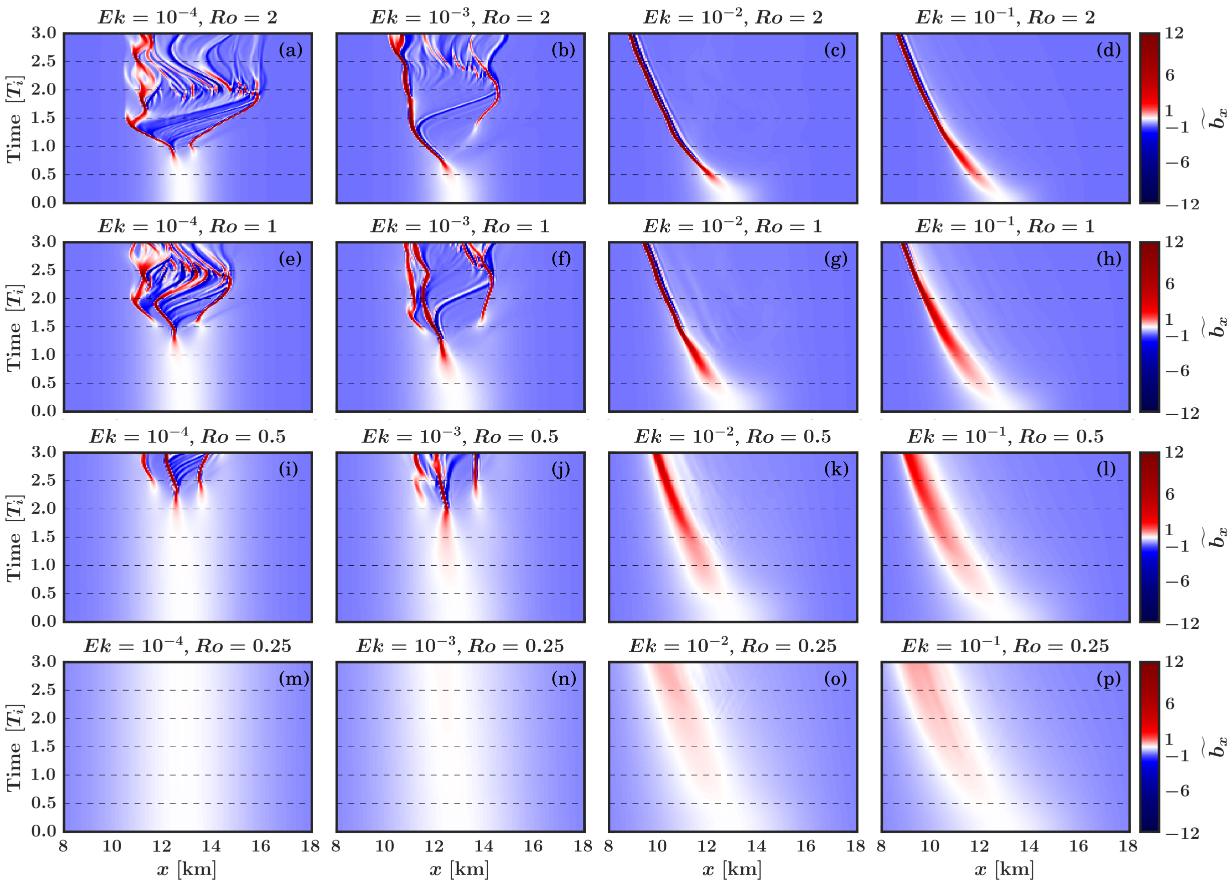

FIG. 5. As in Fig. 3, but for cases with the vertical buoyancy mixing suppressed ($\kappa_v = 0$, $Pr = \infty$; second row, Table 1) Note the sustained frontogenesis ($\widetilde{b_x} >> 0$) in the stronger mixing cases (*e.g.,* $Ek = 10^{-1}$), unlike the frontogenetic inhibition for these cases in Fig. 3 (where $\kappa_v = \nu_v$). All panels share the same, log-scaled colorbar as in Fig. 3.

(Fig. 4b,d) more moderately demonstrate predictive utility of Ro^2/Ek, noting that frontogenesis is primarily a near-surface process.

In Fig. 4a, the frontal sharpening increases with $Ro^2/Ek \gtrsim 50$ and approximately plateaus for $Ro^2/Ek \gtrsim 10^3$, indicating a grid-scale constraint on b_x that occurs at weakest Ek; this trend of increasing frontogenesis for larger Ro^2/Ek also holds when mapping solutions based on $\mathcal{T}_{\text{tot}}$ (Fig. 4c). Note that the cases with SI-induced frontogenesis (*e.g.,* $Ro = 0.5, Ek = 10^{-4}$; Fig. 3i) also approximately collapse on these curves of surface frontogenesis (Fig. 4a,c). In particular this is due to taking maximum b_x and $\mathcal{T}_{\text{tot}}$ over the whole simulation period, which captures very late-stage

($t \approx 4-5\,T_i$) onset of SI *e.g.,* in the $Ro = 0.25, Ek = 10^{-4}$ solution (grey circle in Fig. 4, Fig. 3m). Again, we do not place too much importance on these cases.

We perform an additional test of Ro^2/Ek by running two cases at fixed Ro^2/Ek corresponding to the characteristic frontogenetic case with $Ro = 2$, $Ek = (1.14\times)10^{-2}$ (red star Fig. 4, Fig. 3c). The green ($Ro = 1, Ek = 2.85\times10^{-3}$) and orange ($Ro = 4$, $Ek = 4.56\times10^{-2}$) octagons in Fig. 4 represent these cases with $Ro^2/Ek = 350.87$. Both of these additional cases exhibit frontogenesis analogous to corresponding case in the primary solution set (red star Fig. 4, Fig. 3c), albeit with different time-evolution (not shown). This qualitative agreement in solution behavior further indicates the utility of Ro^2/Ek as a predictor of vertical mixing induced frontogenesis. While the larger Ro case (orange octagon) appears as an outlier relative to the other two cases (red star and green octagon) when measuring maximum b_x relative to the initial condition (Fig. 4a), all three cases exhibit comparable frontal sharpening rates (Fig. 4c,d). The reduced $\max\left[b_x\right]/\max\left[\text{init}.b_x\right]$ for the $Ro = 4$ case (orange octagon Fig. 4a) relative to the other two cases is likely due to the grid-scale constraint on frontogenesis that artificially inhibits frontal sharpening earlier for the large initial $b_x(\propto Ro)$.

The approximate regime collapse on Ro^2/Ek in Fig. 4 is primary result of this study and constitutes an attempted unification of the competing views on the role of vertical mixing in submesoscale frontogenesis (Sec. 1a). In Sec. 5b we discuss how application of a scaling in Crowe and Taylor (2018) (where $D_t b \sim Ro/Ek$) partially succeeds in mapping frontogenesis in our solutions. Because of the idealized setup, particularly the inability of the vertical mixing to respond to the frontal evolution (discussed further in Sec. 5), we do not over-interpret the exact magnitudes in Fig. 4 (*e.g.,* $Ro^2/Ek \sim 50$ as a transition point). Instead, the utility of this parameter mapping is the insight it provides into the governing dynamics of the frontal evolution. That is, because Ro^2/Ek (and not *e.g.,* $1/RoEk$, see Eq. (4a)) appears to explain the solution behavior for all cases with $Pr = 1$, it suggests a strong control on the frontal evolution by the *non-conservative* buoyancy equation. The next section (Sec. 3d) explicitly demonstrates this control of vertical buoyancy mixing on solution behavior via suppression of κ_v.

d. Suppression of vertical buoyancy mixing

Here, we distinguish the role of ν_v and κ_v by suppressing the vertical buoyancy mixing ($\kappa_\text{v} = 0$, $Pr = \infty$) in a twin set of solutions (Table 1). Fig. 5-6 demonstrate frontal evolution in these solutions with $\kappa_\text{v} = 0$ and allow comparison with their counterparts with $\kappa_\text{v} = \nu_\text{v}$. The Hovmöller plots in Fig. 5 are analogous to Fig. 3.

Strikingly, frontogenesis occurs for large Ek and small Ro when $\kappa_\text{v} = 0$ (Fig. 5, right column), remembering that these solutions are frontogenetically inhibited when $\kappa_\text{v} = \nu_\text{v}$ (Fig. 3, right column). In particular, note the *sustained* amplification of $\widetilde{b_x}$ in Fig. 5 for these larger Ek solutions (right two columns). This result explicitly demonstrates that the role of vertical *buoyancy* mixing is to suppress frontogenesis, which is driven by the vertical *momentum* mixing induced ASC. Taking the limit of $Pr \to \infty$ in Eq. (4) offers one explanation for this result. Note that the $Ek = 10^{-4}, 10^{-3}$ cases with buoyancy mixing suppressed (Fig. 5 left two columns) appear similar to their $Pr = 1$ analogs (Fig. 3), suggesting the limited role of κ_v in those solutions with $Pr = 1$.

Fig. 6 compares solutions with $\nu_\text{v} = \kappa_\text{v}$ ($Pr = 1$; solid lines) and $\kappa_\text{v} = 0$ ($Pr = \infty$; dashed lines) at different Ek (colors) and Ro (rows). We plot the time-series of the maximum surface buoyancy gradient (left column) and maximum surface convergence normalized by f (an ASC Rossby number; right column). Again, note the striking, sustained amplification of $\max[b_x]$ for the cases with $\kappa_\text{v} = 0$ compared to their $\nu_\text{v} = \kappa_\text{v}$ counterparts (Fig. 6 left column). For example, note the difference between the black ($Ek = 10^{-1}$) solid ($\kappa_\text{v} = \nu_\text{v}$) and dashed ($\kappa_\text{v} = 0$) lines in Fig. 6a,c,e. For $\kappa_\text{v} = 0$, the frontogenetic rate (*i.e.,* the slope of $\max[b_x]$) is strongest for largest Ro and, interestingly, smaller Ek. Fig. 5 and 6 also demonstrate, particularly at large Ek, that when $\kappa_\text{v} = 0$ frontogenesis continues until reaching the grid-scale, which which occurs earlier and is most apparent at larger Ro. Again, this emphasizes how vertical buoyancy mixing inhibits frontogenesis.

All solutions generally exhibit the same initial growth rate of the the convergence (Fig. 6b,d,f,h) at early time ($t \lessapprox 1\,T_i$). This indicates an inertial control on the initial adjustment (detailed in Sec. 4). The time-series of convergence also show that this initial convergent ASC is strongest for the strongest mixing (largest Ek, black lines). However, in the cases with $\kappa_\text{v} = 0$ (dashed lines), the smaller Ek exhibit stronger later-time frontogenetic rate. That is, the dashed red line in Fig. 6a is larger in magnitude and slope than the dashed black line. This seemingly counter-intuitive trend in Ek for $\kappa_\text{v} = 0$ solutions – stronger frontogenesis for smaller Ek, despite stronger initial convergence

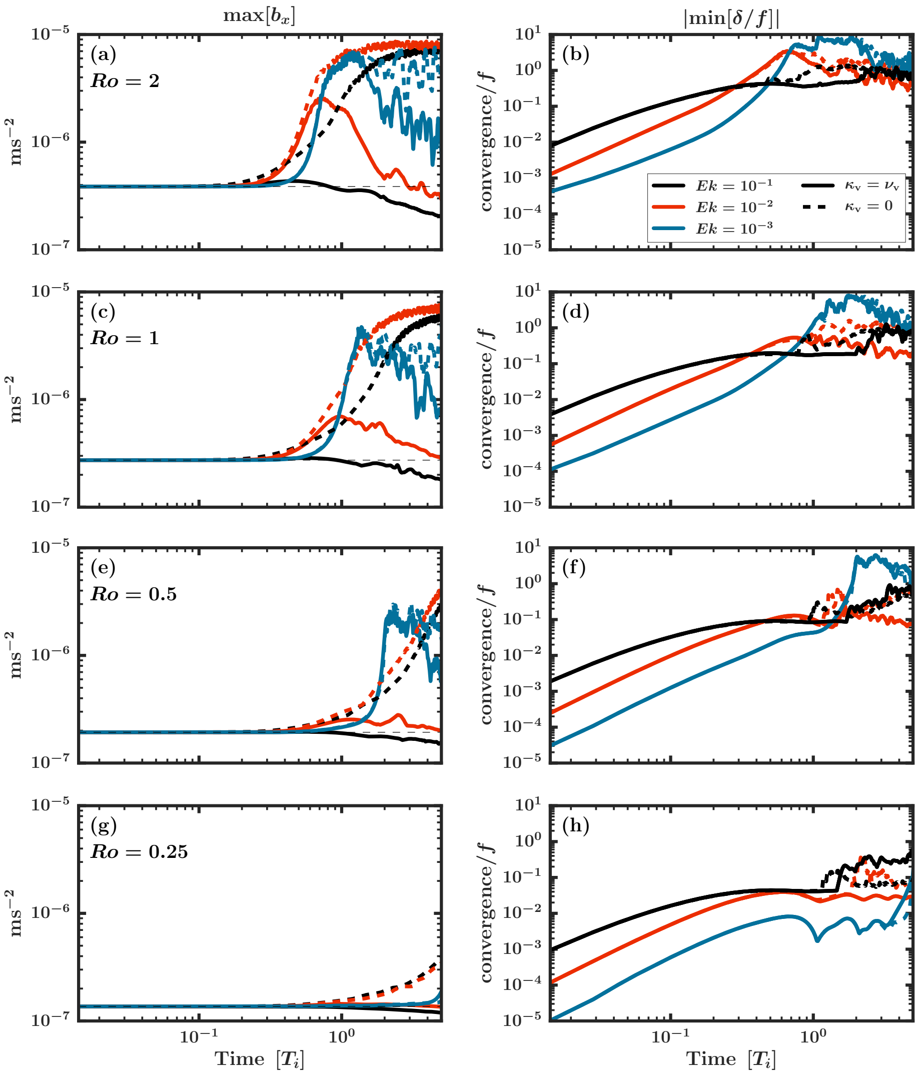

Fig. 6. Demonstration of the impact of vertical buoyancy mixing (κ_v) on frontogenesis with comparison of solutions with $Pr = 1$ ($\kappa_\mathrm{v} = \nu_\mathrm{v}$, solid) and $Pr = \infty$ ($\kappa_\mathrm{v} = 0$, dashed). The panels show time-series of (left) the maximum surface buoyancy gradient and (right) the maximum surface convergence normalized by the Coriolis frequency f for all Ro (rows) at $Ek = 10^{-3}$ (red), $Ek = 10^{-2}$ (blue) and $Ek = 10^{-1}$ (black). The time axis has units of inertial period $T_i = 2\pi/f$. The horizontal dashed line on the left panels indicates the initial condition value, which is the same for each Ro. Note that all the dashed lines ($\kappa_\mathrm{v} = 0$, $Pr = \infty$) exhibit frontogenesis, even at large Ek, and a plateau in b_x (a,b) indicates that the front has reached the grid-scale.

for larger Ek – indicates a frontolytic role of vertical momentum mixing *at later time*, described in Sec. 4.

4. Dynamical balances

Here, we detail controlling dynamical balances from the perspective of buoyancy and momentum evolution. We diagnose terms in various evolutionary equations (defined in Sec. 4a) that collectively demonstrate the mechanisms governing frontal evolution in frontogenetic and frontolytic or frontogenetically inhibited solution regimes (Sec. 3b). We exemplify these mechanisms with detailed analysis of the two characteristic cases in Fig. 2 ($Ro = 2, Pr = 1$ and $Ek = 10^{-1}, 10^{-2}$) as well as their $Pr = \infty$ analogs (Fig. 7-9). The latter allows us to further distinguish the roles of ν_v and κ_v.

A generic, mechanistic description of frontal evolution can be summarized as follows (for $Pr = 1$): vertical momentum mixing induces a convergent ASC via a transient, inertial adjustment – *i.e.,* the linear, transient TTW (or T^{3}W) balance (Wenegrat and McPhaden 2016; Dauhajre and McWilliams 2018; Johnson et al. 2020b) – with Ro, Ek modulating the resulting ASC magnitude and structure. Subsequent frontogenesis, if it occurs, is dominated by nonlinear advection of momentum and buoyancy. Early-stage frontogenetic inhibition or frontolysis (larger Ek) results from vertical buoyancy diffusion that competes comparably with horizontal buoyancy advection. Later-stage frontolysis at smaller Ek can result from inertial oscillations that reverse the ASC. These ASC oscillations weaken the front in a manner that is qualitatively consistent with shear dispersion (Young and Jones 1991; Crowe and Taylor 2018; Wenegrat et al. 2020; Swart et al. 2020), although this is not explicitly diagnosed here.

a. Definitions

The buoyancy frontogenetic tendency equation quantifies the rate of change of the amplitude of the buoyancy gradient ($||\nabla_h b||$) following a fluid parcel (Hoskins 1982). For the 2D system here, $||\nabla_h b|| = b_x$ and the frontogenetic tendency equation is written as:

$$\underbrace{\frac{1}{2} D_t \left(b_x\right)^2}_{\mathcal{T}_\text{tot}} = \underbrace{-b_x b_x u_x}_{\mathcal{T}_u} \underbrace{-b_x b_z w_x}_{\mathcal{T}_w} + \underbrace{b_x \frac{\partial}{\partial x}\left(\frac{\partial}{\partial z}\left(\kappa_\text{v} b_z\right)\right)}_{\mathcal{T}_\text{vmix}} . \tag{6}$$

We diagnose the frontogenetic ($\mathcal{T}_\text{tot} > 0$) and frontolytic ($\mathcal{T}_\text{tot} < 0$) contributions from horizontal advection ($\mathcal{T}_u$), vertical straining ($\mathcal{T}_w$), and vertical diffusion ($\mathcal{T}_\text{vmix}$). In Eq. 6 and other balance

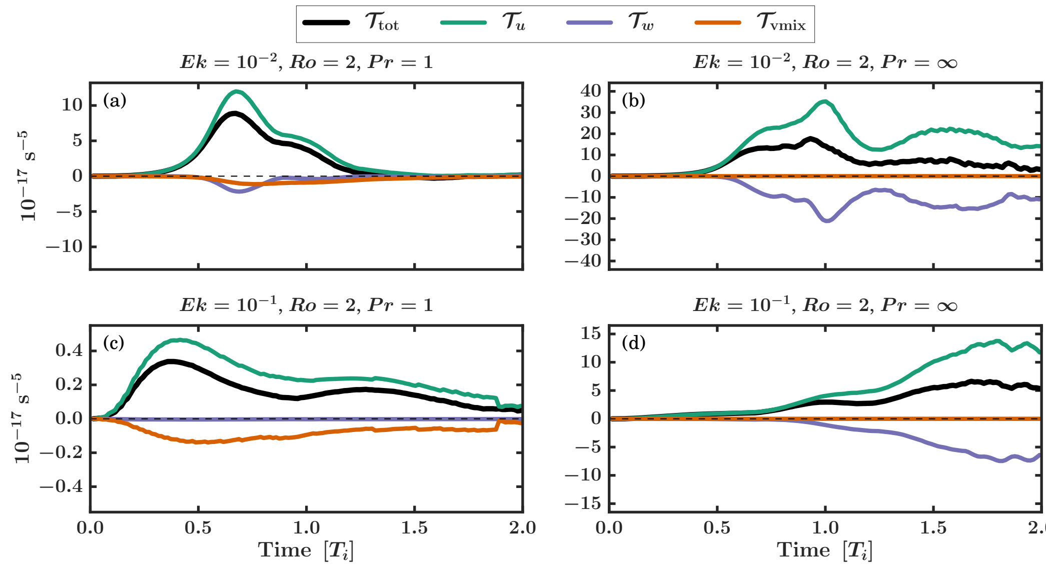

FIG. 7. Time-series of horizontally and vertically averaged buoyancy frontogenetic tendency terms (Eq. 6; terms indicated in the legend) for four cases with initial $Ro = 2$: $Ek = 10^{-2}$ (a,b), $Ek = 10^{-1}$ (c,d) and $Pr = 1$ (a,c) and $Pr = \infty$ (b,d). Here, $\mathcal{T}_{\text{tot}} > 0$ (black) indicates frontogenesis. Note the different y-axis ranges for each panel. Time-series are obtained with spatial averaging in a front-following window that tracks the maximum cross-frontal buoyancy gradient; here, the averaging is done 400 m around the maximum cross-front buoyancy gradient and vertically in the upper ≈ 5 m. Note the strong frontogenesis at $Ek = 10^{-2}$ (a) that is dominated by horizontal advection ($\mathcal{T}_u$); this sharpening is inhibited with stronger buoyancy vertical mixing (c).

equations (defined below), we consider horizontal diffusion negligible. It arises in the present simulations from the implicit hyper-diffusion of the third-order upwind advection scheme and is always frontolytic.

The evolution of the ASC ($\Psi(x,z)$; see Fig. 2) can be described by the cross-front momentum balance (Eq. 7) and the divergence equation (Eq. 8). We diagnose terms in the ageostrophic, cross-front momentum balance as follows:

$$\underbrace{\frac{\partial u}{\partial t}}_{\text{Rate}_u} = \underbrace{-uu_x - wu_z}_{\text{Adv}_u} + \underbrace{f v_{ag}}_{\text{Cor}_{ag,u}} + \underbrace{\frac{\partial}{\partial z}\left(\nu_{\text{v}} u_z\right)}_{\text{Vmix}_u}, \qquad (7)$$

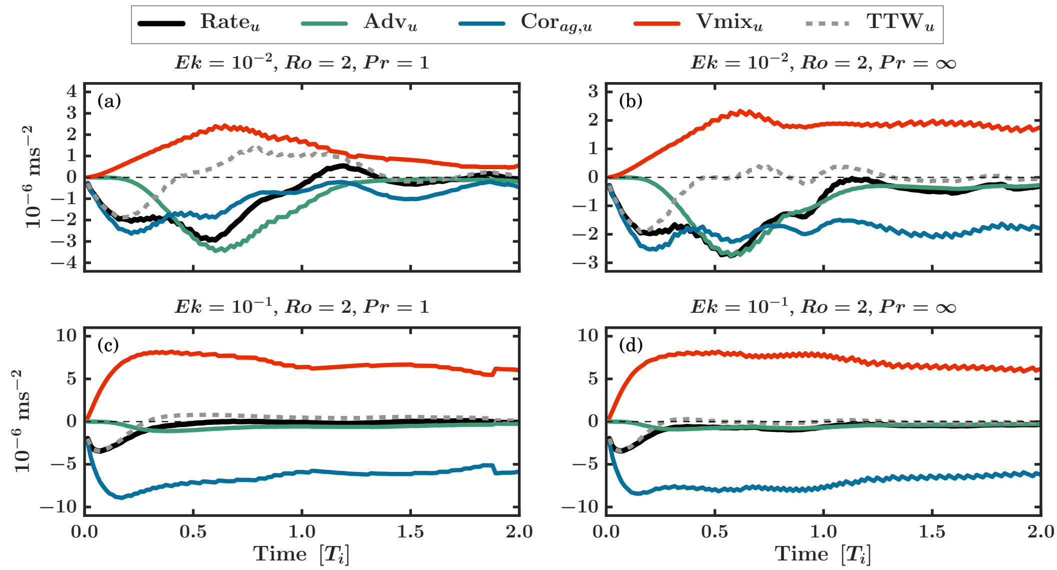

FIG. 8. As in Fig. 7 but for the cross-front momentum balance terms (Eq. (7), terms indicated in the legend). The TTW residual ($\mathrm{TTW}_u = \mathrm{Cor}_{ag,u} + \mathrm{Vmix}_u$) is shown in dashed grey. Here, the time-series are obtained with spatial averaging 400 m around the maximum cross-front buoyancy gradient and vertically in the upper ≈ 2.6 m. Note the transient, linear adjustment in all cases ($\mathrm{Rate}_u \approx \mathrm{Cor}_{ag,u} + \mathrm{Vmix}_u$) in response to vertical momentum mixing breaking geostrophic balance. At smaller Ek (a), momentum advection (green) dominates frontogenesis, while at larger Ek (c) vertical buoyancy diffusion (Fig. 7c) inhibits nonlinear frontogenesis and TTW balance dominates (approximately equal and opposite red and blue curves).

where $\mathrm{Cor}_{ag,u} = f v_{ag} = f v - \phi_x$ is the ageostrophic Coriolis term. We split the material derivative to both isolate the nonlinear contribution (Adv_u) and diagnose the importance of the linear diagnostic TTW balance $\left(\mathrm{Cor}_{ag,u} = -\mathrm{Vmix}_u\right)$ and transient TTW balance (T^{3}W; $\mathrm{Rate}_u = \mathrm{Cor}_{ag,u} - \mathrm{Vmix}_u$).

The divergence equation provides additional, useful perspective on the ASC evolution (with divergence $\delta = u_x$):

$$\underbrace{D_t\delta}_{\mathrm{Rate}_\delta} = \underbrace{-\delta^2}_{\mathrm{Hadv}_\delta} + \underbrace{f\zeta_{ag}}_{\mathrm{Cor}_{ag,\delta}} + \underbrace{w_x u_z}_{\mathrm{Vadv}_\delta} + \underbrace{\frac{\partial}{\partial x}\left(\frac{\partial}{\partial z}\left(\nu_\mathrm{v} u_z\right)\right)}_{\mathrm{Vmix}_\delta} . \tag{8}$$

$\mathrm{Rate}_\delta < 0$ near the surface indicates amplification of a frontogenetic ASC (*i.e.*, intensification of surface convergence), with contributions from horizontal advection (Hadv_δ), the inertial ageostrophic residual $\left(\mathrm{Cor}_{ag,\delta} = f\zeta - \phi_{xx}\right)$, vertical advection ($\mathrm{Vadv}_\delta$), and vertical mixing ($\mathrm{Vmix}_\delta$).

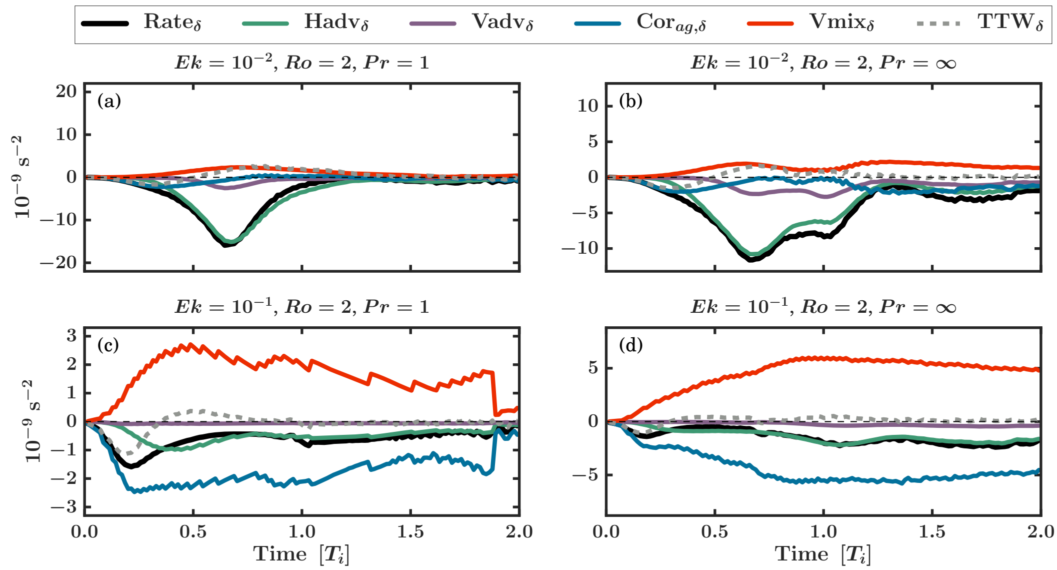

FIG. 9. As in Fig. 7 but for the divergence balance terms (Eq. (8), terms indicated in the legend). The TTW residual ($\mathrm{TTW}_\delta = \mathrm{Cor}_{ag,\delta} + \mathrm{Vmix}_\delta$) is shown in dashed grey. Here, the time-series are obtained with spatial averaging 400 m around the maximum cross-front buoyancy gradient and vertically in the upper ≈ 5 m.

Finally, diagnosis of terms in the vorticity equation (where $\zeta = v_x$) enables insight on the particular role of vertical momentum mixing in breaking geostrophic balance and/or (weakly) inhibiting frontogenesis at later time:

$$\underbrace{D_t\zeta}_{\mathrm{Rate}_\zeta} = \underbrace{-\zeta\delta}_{\mathrm{Hadv}_\zeta} \underbrace{-w_x v_z}_{\mathrm{Vadv}_\zeta} \underbrace{-f\delta}_{\mathrm{Cor}_\zeta} + \underbrace{\frac{\partial}{\partial x}\left(\frac{\partial}{\partial z}(\nu_v v_z)\right)}_{\mathrm{Vmix}_\zeta}, \tag{9}$$

$\mathrm{Rate}_\zeta > 0$ near the surface indicates amplification of the front (increase in cyclonic vorticity) with contributions from vortex stretching (Hadv_ζ), vortex tilting (Vadv_ζ), Coriolis (Cor_ζ) , and vertical mixing (Vmix_ζ).

b. Frontogenetic and frontolytic balances

1) BUOYANCY FRONTOGENETIC TENDENCY

The buoyancy frontogenetic tendency diagnostics (Fig. 7) demonstrate that horizontal buoyancy advection ($\mathcal{T}_u > 0$) drives frontogenesis (here, illustrated for $Ek = 10^{-2}$, green curve, Fig. 7a).

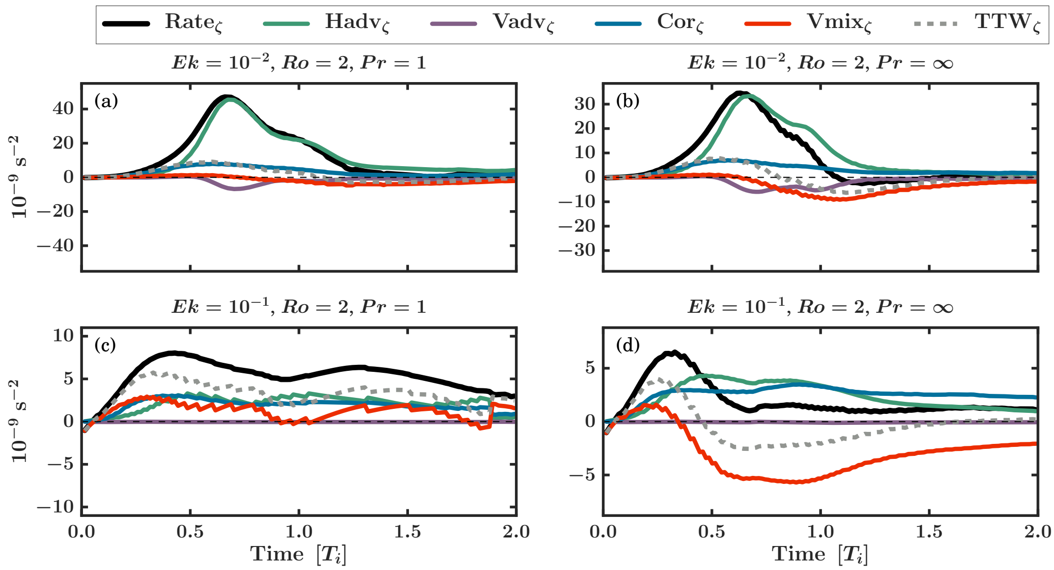

FIG. 10. As in Fig. 7 but for the vorticity balance terms (Eq. (9), terms indicated in the legend). The TTW residual ($\text{TTW}_\zeta = \text{Cor}_\zeta + \text{Vmix}_\zeta$) is shown in dashed grey. The spatial averaging is the same as in Fig. 9.

At stronger mixing ($Ek = 10^{-1}$, Fig. 7b), there is extremely weak advective frontogenesis (note the different y-axis ranges between panels) that competes against the frontolytic impact of vertical mixing ($\mathcal{T}_{\text{vmix}} < 0$; Fig. 7 orange curve), which has comparable in magnitude to $\mathcal{T}_u$.

When buoyancy mixing is suppressed ($Pr = \infty$, Fig. 7b,d), both Ekman number cases exhibit strong frontogenesis driven by horizontal advection ($\mathcal{T}_u > 0$). In these cases, the frontolytic impact of vertical straining ($\mathcal{T}_w < 0$, purple curves) is more apparent, noting that $\mathcal{T}_w < 0$ in a typical, frontogenetic ASC (*e.g.*, Fig. 7a). Note the sustained, increasing frontogenesis in Fig. 7d ($Ek = 10^{-1}, Pr = \infty$), which dominates over the early-time frontogenetic signal that is not visible.

2) Momentum, divergence, and vorticity

Given the geostrophic initial condition (with $v \neq 0$, $\zeta \neq 0$ and $u = w = \delta = 0$) the vertical mixing of geostrophic vorticity ($\text{Rate}_\zeta = \text{Vmix}_\zeta$; Eq. 9) serves as the initial balance-breaking mechanism. This balance-breaking (most apparent in Fig. 10c, red and black curves for $t \sim 0\,T_i$) leads to $\zeta_{ag} \neq 0$, which then influences the cross-front momentum and divergence evolution ($\text{Cor}_{ag,u} \neq 0$ in Eq. 7 and $\text{Cor}_{ag,\delta} \neq 0$ in Eq. 8). Despite this universal balance-breaking mechanism, Fig. 8-10 show a dichotomy in the balances of cross-front momentum, divergence, and vorticity evolution for solutions with weak and strong vertical mixing.

The smaller Ek, frontogenetic solutions (*e.g.,* Fig. 8a,b, 9a,b, and 10a,b) exhibit a three-stage evolution, most apparent in the cross-front momentum balance (Fig. 8a,b): (1) a linear, transient adjustment to balance-breaking via vertical momentum mixing ($\mathrm{Rate}_u \approx \mathrm{Cor}_{ag,u} + \mathrm{Vmix}_u$; the T^{3}W balance); (2) the transition to- and dominance of nonlinear frontogenesis ($\mathrm{Rate}_u \approx \mathrm{Adv}_u$); and (3) later-stage frontolysis resulting from both the weakening of the ASC ($\mathrm{Rate}_u \rightarrow 0$) and vertical buoyancy diffusion (*e.g.,* Fig. 7a, orange curve). The divergence and vorticity balances (Fig. 9a,b, 10a,b) demonstrate that the horizontal advection (green curves) drives the nonlinear frontogenesis ($\mathrm{Rate}_\delta \approx \mathrm{Hadv}_\delta$, $\mathrm{Rate}_\zeta \approx \mathrm{Hadv}_\zeta$), which decreases after approximately $\approx 0.6 - 0.7\ T_i$ (for both $Pr = 1$ and $Pr = \infty$).

It is interesting to note that the trend of $\mathrm{Rate}_u, \mathrm{Rate}_\delta$ and Rate_ζ moving towards zero after this frontogenetic peak appears to follow the nonlinear terms (*i.e.,* agreement between green and black curves after the peak at $t \approx 0.7 - 1.5\ T_i$ in Fig. 8a, 9a, 10a). The approximate agreement between $\mathrm{Cor}_{ag,u}$ and Rate_u in Fig. 8a suggests that later-stage oscillations of the ASC result from inertial oscillations ($\mathrm{Rate}_u \approx \mathrm{Cor}_{ag,u}$), which arise more prominently (less damped) with weaker mixing. Visual inspection of the $Ro = 2, Ek = 10^{-2}, Pr = 1$ case (Fig. 2 top) and other weaker-mixing cases in Movie S1 illustrates that the weakening (and reversals) of the ASC after the initial frontogenetic peak can act to spread the previously sharpened front. We interpret this late-stage frontolysis as analogous to shear dispersion (Young and Jones 1991; Crowe and Taylor 2018; Wenegrat et al. 2020; Swart et al. 2020). However, the shear dispersion spreading rate is inversely proportional to κ_v, and we note that ASC reversals (and later-stage frontal weakening) also occur when buoyancy mixing is suppressed ($Pr = \infty$).

At large Ek (Fig. 8c, 9c), where frontogenesis is inhibited, TTW balance ($\mathrm{Cor}_{ag,u} \approx -\mathrm{Vmix}_u$; $\mathrm{Cor}_{ag,\delta} \approx -\mathrm{Vmix}_\delta$) dominates and there is negligible nonlinearity (see red versus blue curves in both Fig. 8c and 9c). However, there is still a transient adjustment in this case via T^{3}W (agreement between dashed grey and black at very early time); this indicates a generic balance-breaking adjustment, regardless of the mixing amplitude. TTW balance is not as apparent in the vorticity balance for this case (Fig. 10c), indicating some transient, although negligible, evolution of the along-front velocity.

Interestingly, the TTW dominance holds for $Pr = \infty$ at $Ek = 10^{-1}$ (Fig. 8d,9d), indicative of a constraint on momentum advection by strong vertical *momentum* mixing. Note the near constant horizontal advection of divergence ($\mathrm{Hadv}_\delta < 0$) in Fig. 9d that competes against the TTW residual ($\mathrm{TTW}_\delta > 0$; dashed grey). Inspection of the vorticity balance (Fig. 10d) shows that the vertical mixing of vorticity is responsible for this frontogenetic inhibition at larger Ek, even when buoyancy mixing is suppressed. That is, the vertical momentum mixing of the vorticity (red curve Fig. 10d) – as well as the TTW residual (grey curve Fig. 10d) – transition from early-time frontogenetic (amplifying the cyclonic vorticity; $\mathrm{Vmix}_\zeta > 0$) to later-time frontloytic (eroding the geostrophic vertical shear; $\mathrm{Vmix}_\zeta < 0$). This highlights a subtle, relatively weak frontolytic role of vertical momentum mixing at later time, despite its initial role in inducing the frontogenetic ASC.

5. Discussion

a. Instabilities at low Ek

The frontal initial condition (Fig. 1), while designed to be quasi-realistic in structure and magnitude of buoyancy gradients, contains negative potential vorticity (Fig. B1). This negative PV can lead to the onset of (unforced) symmetric instability (SI; Hoskins (1974)), which particularly dominates solution behavior at $Ek = 10^{-4}$ and $Ro = 0.25, 0.5$. We illustrate the onset of SI in one of these weak mixing solutions ($Ro = 0.5$, $Ek = 10^{-4}$, $Pr = 1$; Fig. 11) to exemplify how these motions lead to frontogenesis (*e.g.,* Fig. 3i) and subsequent (improperly resolved) gravitational instability.

Snapshots of overturning circulation qualitatively indicate the onset of SI (Fig. 11a-c). Note that in this solution no discernible ASC develops for $t \lessapprox 2\,T_i$. Instead, multi-signed overturning cells appear after $\approx 2\,T_i$ and align approximately along isopycnals (Fig. 11a), distinct from the single-signed, larger-scale ASC generated via TTW or $\mathrm{T^3W}$ (Fig. 2 top).

We diagnose the geostrophic shear production (GSP; Thomas et al. (2013)) to quantitatively identify these motions as SI, where GSP > 0 indicates SI. GSP is defined as:

$$\mathrm{GSP} = -\overline{v'w'}\frac{\partial \overline{v_g}}{\partial z}\,, \tag{10}$$

where the overbar indicates a horizontal average (for $x > 0$); the primes denote the horizontal anomaly; and v_g the geostrophic, along-front velocity. Fig. 11d-e demonstrates that the emergence

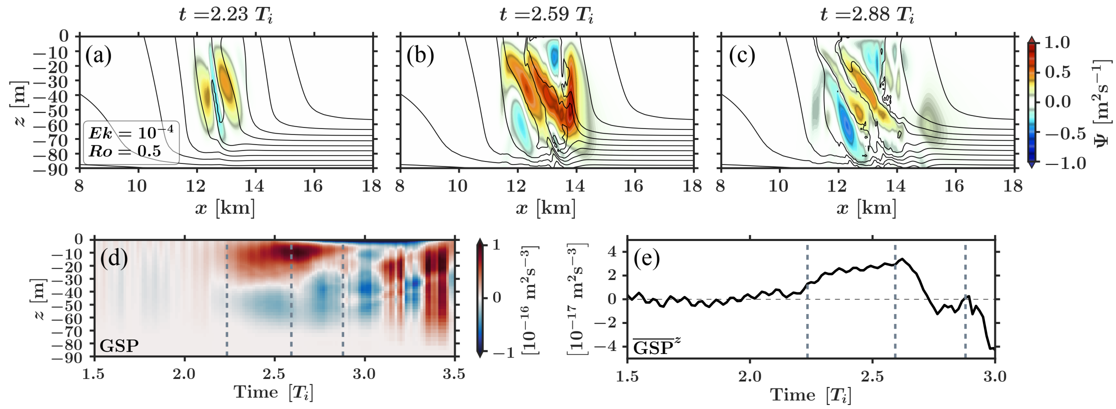

FIG. 11. Example of symmetric instability (SI) in a solution with $Ro = 0.5$, $Ek = 10^{-4}$, $Pr = 1$ (Fig. 3i). (a-c): snapshots of the overturning streamfunction (Ψ) and isopycnals (time indicated at the top of each panel). (d-e) geostrophic shear production (GSP; Eq. 10) as a function of depth and time (d) and vertically averaged in the upper 51 m; GSP is computed in the eastern portion of the domain ($x > 0$; see Fig. 1). The vertical dashed lines in (d-e) indicate the snapshot times in (a-c). Note the approximately along-isopycnal overturning cells in (a-c) – which are structurally distinct from the ASC in Fig. 2 – that occur with GSP > 0 (d-e), indicating the onset of SI. Also note the 'kink' in the mixed layer isopycnals in (a) ($x \approx 13$ km, $z \approx -40$ m), indicating how SI motions create negative stratification, that leads to (improperly resolved) gravitational instability.

of the multi-signed overturning circulation cells are associated with GSP > 0 ($t \approx 2.2 - 2.9\ T_i$), indicating that the unstable motions derive energy from the geostrophic vertical shear.

The multiple overturning cells associated with the onset of SI result in frontogenesis of multiple fronts (most visible in Fig. 11c and Fig. 3i), but also create negative stratification (not shown) that makes the solution gravitationally unstable. Other solutions with low $Ro = 0.25, 0.5$ and low $Ek = 10^{-3}, 10^{-4}$ exhibit variants of this behavior, with onset of SI occurring later for smaller Ro. Additionally, solutions bordering this region of the parameter space can exhibit less intense SI motions along with ASC-driven frontogenesis (*e.g.,* Fig. 3e; see Movie S1).

Symmetric and gravitational instabilities have been observed at fronts in the real ocean (Thomas et al. 2016; Yu et al. 2019; Peng et al. 2021) with measured mixed layer stratification ($N^2 \sim 10^{-5} - 10^{-7}$ s^{-2}) comparable to our initial condition ($N^2 \sim 10^{-7}$ s^{-2}). Verma et al. (2019) demonstrate onset of SI in a 3D LES study simulating the spin-down of a geostrophically balanced front (with initial $Ro = 0.32$); there the (more completely resolved) SI motions result in subsequent shear instabilities, with both symmetric and shear instabilities supplying vertical boundary layer turbulence that induces a re-stratifying, larger-scale secondary circulation. While these and other (Thomas et al. 2013; Bachman et al. 2017; Dong et al. 2021; Chor et al. 2022) studies evidence typicality of symmetric or gravitational instabilities at submesoscale fronts, their emergence in the present solutions, particularly at low Ek, is unconstrained due to the model resolution, hydrostatic assumption, and most importantly, inability of the fixed vertical mixing to respond to these unstable motions. Given the incompleteness of these unstable motions in our simulations, we do not over-interpret the low Ek, low Ro portion of the parameter space (Fig. 3i,j,m,n).

b. Comparisons with past interpretations

The present results reconcile previously competing interpretations (Sec. 1a) of whether and how vertical mixing induces sharpening or weakening of submesoscale fronts, with Fig. 4 (regime collapse on Ro^2/Ek) quantitatively summarizing our attempt at a unified paradigm for this problem. These previous interpretations take the separate views that either momentum dynamics or buoyancy dynamics dominate frontal evolution in response to vertical mixing. The former view anticipates vertical mixing induced frontogenesis via TTW at large Ro (McWilliams et al. 2015; Sullivan and McWilliams 2017, 2024) and the latter anticipates vertical mixing induced frontolysis via shear dispersion or vertical diffusion at small Ro and intermediate to large Ek (Crowe and Taylor 2018, 2019). Our simulations demonstrate all of these frontogenetic or frontolytic mechanisms and we map their relative dominance across a broader (Ek, Ro) space (Fig. 3) compared to previous individual studies (see Table A1).

The identification of Ro^2/Ek as an approximate governor of vertical mixing induced frontogenesis arises from scaling the cross-front velocity as comparable to the along-front velocity at $Ro \sim O(1)$ (as in Barkan et al. (2019)) as well as an identification of fundamental control on solution outcome by competition between cross-front advection of buoyancy and vertical diffusion of buoyancy (Fig. 5, 6). Thompson (2000) highlight this same competition, albeit in a semi-geostrophic framework and with a different scaling (see their Appendix A). Application of the scaling in Crowe and Taylor (2018) gives $D_t b \sim Ro/Ek$ (with $Pr = 1$; see their Eq. 2.1) as opposed to Ro^2/Ek. Ro/Ek exhibits some success for mapping maximum b_x (as in Fig. 4a,b) in our solutions, but does not select for the frontal sharpening rates (as in Fig. 4c,d) as well as Ro^2/Ek (see Fig. 1 in supplemental materials). Fundamentally, both Ro^2/Ek and Ro/Ek quantify the advective (frontogenetic) versus diffusive (frontolytic) competition; Ro^2/Ek assumes a stronger cross-front ageostrophic velocity at $Ro > 1$, which is thought to be more typical of submesoscale fronts with characteristic $Ro \sim O(1-10)$ (Barkan et al. 2019).

While past studies refer to vertical mixing induced frontogenesis as 'TTW frontogenesis' (McWilliams et al. 2015), the TTW balance in the present simulations is only valid in frontogenetically inhibited cases with large Ek (Fig. 8c). In our simulations, a linear, transient adjustment creates the frontogenetic secondary circulation (Fig. 8a) that transitions to a nonlinear balance during peak frontogenesis. Of course, this transient adjustment is a consequence of the geostrophic initial condition, however, we note that simulations with an initial condition in TTW balance (not shown) behave analogously.

We primarily focus on early-time solution behavior ($t \lessapprox 2$ inertial periods), noting the super-inertial nature of submesoscale frontogenesis (Barkan et al. 2019). This early-time focus contrasts with the long-time ($t \gtrapprox 10$ inertial periods) focus of Crowe and Taylor (2018, 2019, 2020) (and their theoretical predecessor (Young 1994)). The transience of early-time frontogenesis in the present simulations (Fig. 6 solid curves) is, however, qualitatively consistent with the even more idealized simulations in Crowe and Taylor (2019) (see their Fig. 7), which initialize a front with zero vertical stratification and employ a free-slip bottom and uniform mixing. Crowe and Taylor (2019) partially interpret this behavior at $Ro = 1$ to result from the development of a depth-uniform geostrophic jet that forms on the edges of their idealized front. These dynamics do not appear relevant in our simulations, likely due to differences in our time-period of interest, initial condition, and bottom boundary condition. Here, we observe that momentum advection and convergence dominate our strongest frontogenetic cases (Fig. 8a, 9a), with this frontogenesis occurring for $\lessapprox 1$ inertial period. This result corroborates the inviscid, asymptotic model of Barkan et al. (2019), which predicts that the surface convergence of the ASC (as opposed to deformation) dominates the frontogenetic tendency of buoyancy (Fig. 7), divergence (Fig. 9), and vorticity (Fig. 10).

When $Pr = 1$, vertical mixing induced frontogenesis does not 'run away' to a singularity, as anticipated in inviscid theory for strain-induced frontogenesis (Hoskins and Bretherton 1972) and some interpretations of TTW frontogenesis (Sec. 6 in McWilliams et al. (2015)). Instead, the temporally fixed vertical buoyancy diffusion acts as the primary inhibitor of frontal sharpening. This frontal weakening by κ_v occurs via vertical diffusion at early-time (large Ek; Fig. 7c) or via shear dispersion at later time (small Ek), where inertial oscillations of the cross-frontal flow aid in spreading the previously sharpened front (see Movie S1). While Wenegrat et al. (2020) evidences shear dispersion at submesoscale fronts in the Gulf Stream, the late-time inertial oscillations (and associated frontal spreading) in our simulations may result artificially from the fixed mixing assumption and 2D posing; the fixed mixing limits the ability of the (weak) vertical mixing to damp inertial oscillations and the 2D posing excludes 3D instabilities (*e.g.,* baroclinic mixed layer, horizontal shear) that may preclude these late-stage inertial oscillations (discussed further in Sec. 5c).

As in Bodner et al. (2019), we attempt to distinguish the roles of ν_v and κ_v in sharpening or weakening fronts, albeit with a different approach. Bodner et al. (2019) treat the vertical mixing as a first-order correction to inviscid, strain-induced frontogenesis theory (Shakespeare and Taylor 2013), while we prescribe the vertical eddy viscosity and diffusivity in a primitive equation system with no straining. In our posing, the vertical eddy viscosity is necessary for inducing the ASC and initiating frontogenesis, which is in contrast to Bodner et al. (2019) who find that ν_v weakens the strain-driven frontogenesis. However, we also demonstrate that ν_v actually inhibits frontogenesis at later time via mixing of the along-front velocity and vorticity (Fig. 10d). We do not observe that κ_v enhances frontogenesis, in contrast to Bodner et al. (2019), who observe frontogenetic enhancement by κ_v at later-time; although, they note this later-time is beyond the limit of the perturbation approach.

c. Applicability of interpretations to submesoscale fronts in nature

A utility of this study is the prediction of frontal evolution given a measure of frontal strength (Ro) and vertical mixing intensity (Ek), with Ro^2/Ek quantifying the competition between cross-front buoyancy advection and vertical diffusion that approximately governs solution outcome (Fig. 4). This competition could be measured locally at a front as:

$$\frac{Ro^2}{Ek} \approx \frac{\zeta^2 h_{ml}^2}{\kappa_\mathrm{v} f} \quad \text{or} \quad \frac{\delta^2 h_{ml}^2}{\kappa_\mathrm{v} f} \,. \tag{11}$$

While this metric could potentially explain whether real submesoscale fronts sharpen or weaken, the exclusion of other intrinsic processes in the idealized posing may limit applicability of our interpretations to the real ocean. These additional processes primarily include the response of vertical mixing to frontal evolution, straining or deformation flows, and 3D instabilities.

The fixed vertical mixing assumption allows us to treat Ro and Ek as independent parameters in the present idealized framework. In reality, Ro and Ek are not independent; the boundary layer turbulence (Ek) evolves spatially and temporally in response to the frontal evolution (Ro) and vice versa. We illustrate the spatial variability of Ek at submesoscale fronts and filaments in a realistically configured simulation in Fig. 2 of the supplementary materials, leaving comprehensive investigation of Ro and Ek dependencies in such simulations for future work. Past numerical studies of submesoscale dense filaments – with both partially resolved (Sullivan and McWilliams 2017, 2024) and parameterized (Gula et al. 2014; McWilliams et al. 2015) vertical boundary layer turbulence – demonstrate a horizontal structure in vertical mixing: stronger mixing at the filament center relative the surrounding, re-stratified regions. The spatio-temporal response of the vertical mixing to frontal evolution may alter the (late-time) frontolytic behavior in the present idealizations, which results from a fixed vertical eddy diffusivity and/or inertial oscillations (Sec. 4). Vertical buoyancy mixing that reaches further into the pycnocline, relative to our posing (Fig. 1e), can mix stratified water into the mixed layer and accelerate frontolysis. More generally, spatial structure in the vertical boundary layer turbulence raises questions regarding the utility or most dynamically apt definition of Ek at a front or filament

Straining currents can induce or maintain the frontogenetic secondary circulation, separate from vertical momentum mixing via TTW (or transient TTW). This straining can be supplied by mesoscale currents or submesoscale mixed layer eddies (Boccaletti et al. 2007; Zhang et al. 2021). While Bodner et al. (2019) attempt to diagnose the relative roles of straining and vertical mixing during 2D frontogenesis, there remains an open question regarding the role of these processes at different stages in a frontal life-cycle. A less-highlighted, but relevant result of this study is the demonstration that temporally fixed vertical mixing does not induce frontogenesis for initial $Ro = 0.25$ (Fig. 3m-p, excluding the very late-time SI induced frontogenesis in m,n; see Sec. 5a). This result indirectly suggests that either straining currents or vertical mixing response to the front are required to drive a transition from $Ro \sim 0.1$ to $Ro >> 1$. However, this view assumes that submesoscale fronts 'start' with a particular (mesoscale or mixed layer eddy) Ro and motivates clarification on 'typical' precursor conditions to frontogenesis.

Along-front, horizontal shear instabilities (Sullivan and McWilliams 2024; Wu et al. 2022; Gula et al. 2014) provide a separate route to frontal erosion or arrest that can preclude the vertical diffusion or shear dispersion frontolytic mechanisms demonstrated in this 2D study. The respective roles of vertical buoyancy diffusion and instabilities (horizontal shear, vertical shear, centrifugal, symmetric) in driving frontolysis remain to be systematically quantified, while also noting that some of these instabilities can actually set up the ASC as demonstrated in Verma et al. (2019). The expectation is that the competition between the vertical mixing rate ($h_{ml}^2/\kappa_{\mathrm{v}}$) and the growth rate of the instability – both of which compete with (or contribute to; Verma et al. (2019)) frontogenesis by the secondary circulation – determines the dominant frontolytic mechanism.

Recent observations (Swart et al. 2020) and realistic simulations (Sun et al. 2020) demonstrate that strong winds can erode submesoscale fronts, with Swart et al. (2020) suggesting shear dispersion via inertial oscillations as a frontolytic mechanism initiated by winds. While we capture analogous behavior in our simulations, particularly at lower Ek (Sec. 4), our results demonstrate that strong vertical buoyancy diffusion also drives frontolysis (at small Ro^2/Ek). This motivates further work to diagnose the relative roles of vertical diffusion and shear dispersion during strong wind events. Absent from these frontolytic paradigms is the consideration of favorably aligned wind-stresses that can drive frontogenesis (Crowe and Taylor 2020) as well as wind-driven across-front buoyancy fluxes that create conditions for symmetric instabilities (Thomas et al. 2013, 2016). Such instabilities will enhance localized mixing ($\nu_{\mathrm{v}}, \kappa_{\mathrm{v}}$), but may also initiate a transition to 3D, frontolytic instabilities (*e.g.,* horizontal shear instability) as described above. This interplay remains relatively unexplored.

d. Implications for submesoscale parameterization

Recently designed parameterization of submesoscale re-stratification fluxes rely on assumption that the steady-state TTW balance well-predicts either the width of "stable" fronts (Bodner et al. 2023) or the submesoscale secondary circulation and thus re-stratification (Yang et al. 2024). This study demonstrates that non-steady and nonlinear dynamics dominate re-stratification during frontogenesis (Sec. 4). In the present simulations, the TTW balance is only valid in the frontogenetically inhibited cases (Fig. 8c). This result partially supports an interpretation that TTW controls the 'arrested' frontal width (Bodner et al. 2023), while noting that vertical buoyancy diffusion primarily drives frontolysis in these large Ek cases (Fig. 7c; Fig. 6a black curve). More generally, the present demonstrations of non-steady momentum and buoyancy balances – whether during linear secondary circulation adjustment, nonlinear frontogenesis, or vertical buoyancy diffusion driven frontolysis – motivate consideration of transient dynamics in designing parameterization of submesoscale fluxes, while noting the caveats of the idealization (Sec. 5c).

6. Summary and conclusions

This study re-litigates the role of vertical mixing in submesoscale frontogenesis and frontolysis (Sec. 1a) with a suite of idealized simulations (Fig. 3,5; Table 1) that evolve 2D fronts initially in geostrophic balance over a range of initial frontal strengths (Ro) and vertical mixing intensities (Ek), where the introduction of vertical mixing (ν_v, κ_v) triggers a frontal evolution. Our problem posing (Sec. 2) prescribes an initial surface mixed layer front that is guided by realism (in Ro and stratification); however, in order to explicitly isolate the role of vertical mixing, we artificially hold the vertical eddy viscosity and diffusivity profiles (Fig. 1e) as constant in time.

We observe that vertical mixing can both induce and inhibit frontogenesis (focusing on the first $\approx 1-2$ inertial periods; Fig. 3), with Ro^2/Ek (Fig. 4) approximately mapping regime transitions (for solutions with $\nu_v = \kappa_v$; Table 1); this parameter quantitatively signifies our attempt at a common paradigm for this problem. Ro^2/Ek measures the competition between cross-front buoyancy advection and vertical diffusion and reflects a particular scaling choice (originally proposed in Barkan et al. (2019); Sec. 2b) that captures the strong ageostrophic secondary circulation that drives submesoscale frontogenesis with typical $Ro > 1$. We also note the potential applicability of an analogous parameter (Ro/Ek) utilizing the scaling of Crowe and Taylor (2018) (see Sec. 5b), despite its theoretical limitation to $Ro < 1$.

The controlling dynamics elucidated in this study blend and update previous interpretations of vertical mixing impacts on submesoscale frontogenesis: turbulent thermal wind (TTW) frontogenesis and shear dispersion or vertical diffusion frontolysis (Sec. Sec. 1a and 5b). For large Ro^2/Ek, vertical momentum mixing can induce a transition to nonlinear, convergence dominated (Barkan et al. 2019) frontogenesis via the generation of an ageostrophic secondary circulation (McWilliams et al. 2015; McWilliams 2017; Sullivan and McWilliams 2017, 2024). Conversely, for small Ro^2/Ek, vertical buoyancy mixing suppresses frontogenesis via strong vertical diffusion that inhibits frontal sharpening by the secondary circulation (Crowe and Taylor 2018, 2019). This distinction between the generally frontogenetic impact of ν_v and solely frontolytic impact of κ_v is made explicit with simulations that set $\kappa_v = 0$ (Fig. 5), which all exhibit frontogenesis, remarkably, even at large Ek. In all simulations, transient TTW dynamics (Wenegrat and McPhaden 2016; Dauhajre and McWilliams 2018) – as opposed to the usually-invoked diagnostic TTW balance (Garrett and Loder 1981; Gula et al. 2014; McWilliams et al. 2015; McWilliams 2017) – generate the secondary circulation; we observe that TTW balance is valid only in the frontogenetically inhibited cases (Fig. 8, Sec. 4) or unrealistically frontogenetic cases with $\kappa_v = 0$ (Fig. 5), particularly at large Ek.

We expect similar results for submesoscale dense filaments, a common (McWilliams et al. 2015; McWilliams 2017; Sullivan and McWilliams 2017, 2024) and dynamically relevant target for this problem. We note that Sullivan and McWilliams (2024) observe weak-to-no frontogenesis for an initially weak dense filament that is subject to strong atmospheric cooling; this is qualitatively consistent with the small Ro, large Ek outcome here.

The present simulations also exhibit late-stage ($\gtrsim 1.5 - 2$ inertial periods) frontolysis at larger Ro^2/Ek (after early-time frontogenesis) that is qualitatively consistent with shear dispersion (Young and Jones 1991; Crowe and Taylor 2018; Wenegrat et al. 2020; Swart et al. 2020) as well as frontogenesis induced by symmetric instability (Verma et al. 2019) at very small Ek, Ro (*e.g.,* Fig. 3i). However, we caution interpretation of these regimes due to the fixed vertical mixing assumption that limits solution validity at later-time (Sec. 5a,c). More generally, the assumption of fixed vertical mixing in this study places a fundamental limitation on extrapolating the present interpretations to submesoscale fronts nature, where Ro and Ek are not independent. Future work can interrogate the applicability of the present idealized framework (*e.g.,* predictive utility of Ro^2/Ek) in more realistic scenarios.

Acknowledgments. D.P. Dauhajre, D. Hypolite and J.C. McWilliams were supported by the National Science Foundation (NSF) grant OCE-2124174 and the Office of Naval Research (ONR) grant N00014-23-1-2812. J. Gula was supported by the French National Agency for Research (ANR) through the project DEEPER (ANR-19-CE01-0002-01), and by ONR grant N00014-23-1-2226.

Data availability statement. The simulations in this study are run with the UCLA ROMS code: https://github.com/CESR-lab/ucla-roms. Setup files for the idealized double front configuration are available at: https://github.com/ddauhajre/IdealFrontVmixROMS

APPENDIX A

Inventory of past numerical and theoretical studies

Table A1 summarizes the (Ek, Ro) parameter space of past idealized modeling or theoretical studies that investigate the role of vertical mixing in submesoscale frontogenesis. This table is provided as context for the discussion in Sec. 1 and 5.

TABLE A1. Summary of past numerical and theoretical studies that investigate vertical mixing impacts on frontogenesis. The listed values of Ro (of either an initial condition or applicability in theory) and Ek are either reported in the studies or estimated here, with blank values indicating that Ro or Ek are either not reported and/or difficult to estimate (*e.g.,* for Large eddy simulations).

Study	Approach	Ro	Ek	Vertical mixing representation
Thompson (2000)	Semi-geostrophic model	< 0.1		constant
McWilliams et al. (2015)	2D primitive equation model	≈ 2	$\approx 0.05 - 0.1$	K-profile parameterization
McWilliams (2017)	TTW+Omega equation diagnostics	$\lessapprox 1$	$\approx 0.05 - 0.1$	analytical formulation
Sullivan and McWilliams (2017)	3D Large eddy simulation	$\gtrapprox 1$		partially resolved
Crowe and Taylor (2018, 2020)	Asymptotic theory	< 1	O(1), O(Ro)	constant
Crowe and Taylor (2019)	2D Large eddy simulation	$0.1 - 1$	$0.01 - 1$	constant
Bodner et al. (2019)	Perturbation analysis	0.4		first-order correction to strain theory
Verma et al. (2019)	3D Large eddy simulation	0.32		partially resolved
Sullivan and McWilliams (2024)	3D Large eddy simulation	$0.3 - 4$		partially resolved

APPENDIX B

Idealized initial condition and vertical mixing profile

The double front initial condition (Fig. 1) prescribes a 2D buoyancy field ($b(x,z)$) and associated geostrophic (along-front) velocity ($v(x,z)$). Fig. B1 shows the potential vorticity of the initial condition for each Ro. Negative potential vorticity ($q = (v_x + f)b_z - |b_x|^2/f$) in the initial condition – a consequence of quasi-realistic b_z, b_x – leads to the onset of symmetric instability in cases with weak mixing (see Sec. 5a).

The construction of $b(x,z)$ follows McWilliams (2017):

$$b(x,z) = b_0 + N_b^2\,(z+H) + \frac{N_0^2}{2}\left[(1+B)\,z - (1-B)\left(h_{ml}(x) + \lambda^{-1}\log\cosh\left[\lambda(z+h_{ml}(x))\right)\right]\right]. \quad \text{(B1)}$$

where N_b^2 is a minimum background stratification, N_0^2 the interior stratification, λ a scale of the transition between the surface boundary layer and interior stratification that exhibits a fractional reduction in stratification of B.

The mixed layer depth ($h_{ml}(x)$) sets the double front structure (shape and magnitude of b_x):

$$h_{ml}(x) = h_0 + \delta h\left[\tanh(M_f(x-x_f)) - \tanh(M_f(x+x_f))\right], \quad \text{(B2)}$$

where h_0 is the mixed layer depth away from the front; $h_0 + \delta_h$ the mixed layer depth at the front; and $\pm x_f$ the location of the front. We modulate the initial frontal strength (Ro in Fig. 1a-d) via M_f in Eq. B2; we set $M_f = \left[3.11\times10^{-4}, 4.4\times10^{-4}, 6.24\times10^{-4}, 8.83\times10^{-4}\right]$ m^{-1} for $Ro = [0.25, 0.5, 1, 2]$, respectively.

We set the following (in all simulations) relative to Eq. B1-B2:

$$b_0 = 5\times10^{-2}\ \mathrm{ms}^{-2}, \quad B = 0.025 \quad \text{(B3)}$$

$$N_0^2 = 3\times10^{-5}\ \mathrm{s}^{-2}, \quad N_b^2 = 10^{-7}\ \mathrm{s}^{-2}, \quad \lambda^{-1} = 8\ \mathrm{m} \quad \text{(B4)}$$

$$h_0 = 60\ \mathrm{m}, \quad \delta_h = 15\ \mathrm{m}, \quad x_f = 12.8\ \mathrm{km} \quad \text{(B5)}$$

The prescribed vertical mixing profile ($\nu_\mathrm{v} = \kappa_\mathrm{v}$) is cubic and non-zero only above a threshold mixed layer depth ($h^*_{ml} = 70$ m):

$$\nu_\mathrm{v}(z) = \nu_{\max}\frac{z'\,(1-z')^2}{0.14805} \quad \text{(B6)}$$

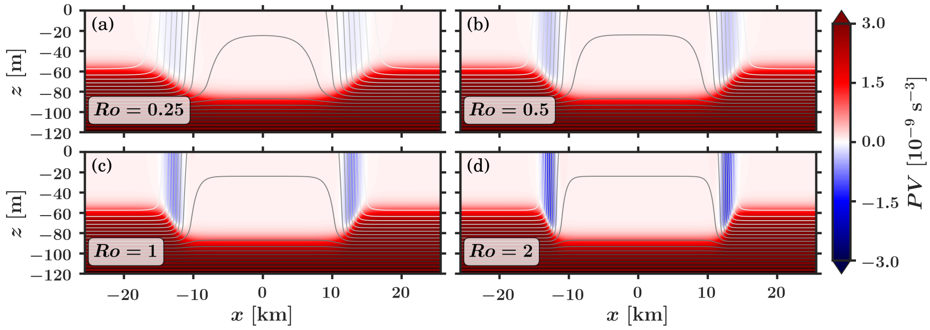

FIG. B1. Potential vorticity $q = (v_x + f)b_z - |b_x|^2/f$ for the four Ro double front initial conditions, as in Fig. 1.

where $z' = \frac{\eta - z}{h^*_{ml}}$ and $\nu_{\max}$ sets the magnitude (and thus Ek). For $f = 10^{-4}$ and $h_{ml} = 70$ m, we set $\nu_{\max} = \left[10^{-4}, 10^{-3}, 10^{-2}, 10^{-1}\right]$ m^{2}s^{-1} to give $Ek = 1.14 \times \left[10^{-4}, 10^{-3}, 10^{-2}, 10^{-1}\right]$, where the 1.14 factor comes from the vertical average of $\frac{\nu_v(z)}{\nu_{\max}}(= 0.56)$ in the upper 70 m.

References

Bachman, S., B. Fox-Kemper, J. Taylor, and L. Thomas, 2017: Parameterization of frontal symmetric instabilities. i: Theory for resolved fronts. *Ocean Modelling*, **109**, 72–95, https://doi.org/https://doi.org/10.1016/j.ocemod.2016.12.003.

Bachman, S. D., and J. R. Taylor, 2016: Numerical simulations of the equilibrium between eddy-induced restratification and vertical mixing. *Journal of Physical Oceanography*, **46 (3)**, https://doi.org/10.1175/JPO-D-15-0110.1.

Barkan, R., M. Molemaker, K. Srinivasan, J. McWilliams, and E. D‘Asaro, 2019: The role of horizontal divergence in submesoscale frontogenesis. *J. Phys. Oceanogr.*, **49**, 1593–1618, https://doi.org/10.1175/JPO-D-18-0162.1.

Boccaletti, G., R. Ferrari, and B. Fox-Kemper, 2007: Mixed layer instabilities and restratification. *J. Phys. Oceanogr.*, **37**, 2228–2250, https://doi.org/10.1175/JPO3101.1.

Bodner, A. S., B. Fox-Kemper, L. Johnson, L. P. V. Roekel, J. C. McWilliams, P. P. Sullivan, P. S. Hall, and J. Dong, 2023: Modifying the mixed layer eddy parameterization to include frontogenesis arrest by boundary layer turbulence. *Journal of Physical Oceanography*, **53 (1)**, 323 – 339, https://doi.org/10.1175/JPO-D-21-0297.1.

Bodner, A. S., B. Fox-Kemper, L. P. VanRoekel, J. C. McWilliams, and P. P. Sullivan, 2019: A perturbation approach to understanding the effects of turbulence on frontogenesis. *Journal of Fluid Mechanics*, **883**, A25, https://doi.org/10.1017/jfm.2019.804.

Buckingham, C. E., N. S. Lucas, S. E. Belcher, T. P. Rippeth, A. L. M. Grant, J. Le Sommer, A. O. Ajayi, and A. C. Naveira Garabato, 2019: The contribution of surface and submesoscale processes to turbulence in the open ocean surface boundary layer. *Journal of Advances in Modeling Earth Systems*, **11 (12)**, 4066–4094, https://doi.org/https://doi.org/10.1029/2019MS001801.

Carpenter, J. R., A. Rodrigues, L. K. P. Schultze, L. M. Merckelbach, N. Suzuki, B. Baschek, and L. Umlauf, 2020: Shear instability and turbulence within a submesoscale front following a storm. *Geophysical Research Letters*, **47 (23)**, e2020GL090 365, https://doi.org/https://doi.org/10.1029/2020GL090365.

Chor, T., J. O. Wenegrat, and J. Taylor, 2022: Insights into the mixing efficiency of submesoscale centrifugal–symmetric instabilities. *Journal of Physical Oceanography*, **52 (10)**, 2273 – 2287, https://doi.org/https://doi.org/10.1175/JPO-D-21-0259.1.

Crowe, M. N., and J. R. Taylor, 2018: The evolution of a front in turbulent thermal wind balance. part 1. theory. *Journal of Fluid Mechanics*, **850**, 179–211, https://doi.org/10.1017/jfm.2018.448.

Crowe, M. N., and J. R. Taylor, 2019: The evolution of a front in turbulent thermal wind balance. part 2. numerical simulations. *Journal of Fluid Mechanics*, **880**, 326–352, https://doi.org/10.1017/jfm.2019.688.

Crowe, M. N., and J. R. Taylor, 2020: The effects of surface wind stress and buoyancy flux on the evolution of a front in a turbulent thermal wind balance. *Fluids*, **5 (2)**, https://doi.org/10.3390/fluids5020087.

Damien, P., D. Bianchi, J. C. McWilliams, F. Kessouri, C. Deutsch, R. Chen, and L. Renault, 2023: Enhanced biogeochemical cycling along the u.s. west coast shelf. *Global Biogeochemical Cycles*, **37 (1)**, e2022GB007 572, https://doi.org/https://doi.org/10.1029/2022GB007572.

Dauhajre, D. P., and J. McWilliams, 2018: Diurnal evolution of submesoscale front and filament circulations. *J. Phys. Oceanogr.*, **48**, 2343–2361, https://doi.org/10.1175/JPO-D-18-0143.1.

Dauhajre, D. P., J. McWilliams, and Y. Uchiyama, 2017: Submesoscale Coherent Structures on the Continental Shelf. *J. Phys. Oceanogr.*, **47**, 2949 – 2976, https://doi.org/10.1175/JPO-D-16-0270.1.

Dong, J., B. Fox-Kemper, H. Zhang, and C. Dong, 2021: The scale and activity of symmetric instability estimated from a global submesoscale-permitting ocean model. *Journal of Physical Oceanography*, **51 (5)**, 1655 – 1670, https://doi.org/10.1175/JPO-D-20-0159.1.

D'Asaro, E. A., and Coauthors, 2018: Ocean convergence and the dispersion of flotsam. *Proceedings of the National Academy of Sciences*, **115 (6)**, 1162–1167, https://doi.org/10.1073/pnas.1718453115.

Fahlbusch, J. A., D. E. Cade, E. L. Hazen, M. L. Elliott, B. T. Saenz, J. A. Goldbogen, and J. Jahncke, 2024: Submesoscale coupling of krill and whales revealed by aggregative lagrangian coherent structures. *Proc. R. Soci. B.*, **291 (20232461)**, https://doi.org/10.1098/rspb.2023.2461.

Farrar, J. T., and Coauthors, 2020: S-mode: The sub-mesoscale ocean dynamics experiment. *IGARSS 2020 - 2020 IEEE International Geoscience and Remote Sensing Symposium*, 3533–3536, https://doi.org/10.1109/IGARSS39084.2020.9323112.

Fox-Kemper, B., R. Ferrari, and R. Hallberg, 2008: Parameterization of mixed layer eddies. part i: Theory and diagnosis. *Journal of Physical Oceanography*, **38 (6)**, 1145 – 1165, https://doi.org/10.1175/2007JPO3792.1.

Fox-Kemper, B., and Coauthors, 2011: Parameterization of mixed layer eddies. iii: Implementation and impact in global ocean climate simulations. *Ocean Modelling*, **39 (1)**, 61–78, https://doi.org/https://doi.org/10.1016/j.ocemod.2010.09.002.

Freilich, M. A., G. Flierl, and A. Mahadevan, 2022: Diversity of growth rates maximizes phytoplankton productivity in an eddying ocean. *Geophysical Research Letters*, **49 (3)**, e2021GL096 180, https://doi.org/https://doi.org/10.1029/2021GL096180.

Garrett, C., and J. Loder, 1981: Dynamical aspects of shallow sea fronts. *Phil. Trans. R. Soc. Lond.*, **302**, 563–581, https://doi.org/10.1098/rsta.1981.0183.

Gula, J., M. Molemaker, and J. McWilliams, 2014: Submesoscale cold filaments in the Gulf Stream. *J. Phys. Oceanogr.*, **44**, 2617–2643, https://doi.org/10.1175/JPO-D-14-0029.1.

Gula, J., J. Taylor, A. Shcherbina, and A. Mahadevan, 2022: Chapter 8 - Submesoscale processes and mixing. *Ocean Mixing*, M. Meredith, and A. Naveira Garabato, Eds., Elsevier, 181–214, https://doi.org/10.1016/B978-0-12-821512-8.00015-3.

Heaps, N. S., 1972: Estimation of Density Currents in the Liverpool Bay Area of the Irish Sea. *Geophysical Journal International*, **30 (4)**, 415–432, https://doi.org/10.1111/j.1365-246X.1972.tb05825.x.

Hoskins, B. J., 1974: The role of potential vorticity in symmetric stability and instability. *Quarterly Journal of the Royal Meteorological Society*, **100 (425)**, 480–482, https://doi.org/https://doi.org/10.1002/qj.49710042520.

Hoskins, B. J., 1982: The mathematical theory of frontogenesis. *Ann. Rev. Fluid Mech.*, **14**, 131–151, https://doi.org/10.1146/annurev.fl.14.010182.001023.

Hoskins, B. J., and F. P. Bretherton, 1972: Atmospheric frontogenesis models: Mathematical formulation and solution. *Journal of Atmospheric Sciences*, **29 (1)**, 11 – 37, https://doi.org/https://doi.org/10.1175/1520-0469(1972)029⟨0011:AFMMFA⟩2.0.CO;2.

Johnson, L., C. M. Lee, E. A. D'Asaro, L. Thomas, and A. Shcherbina, 2020a: Restratification at a california current upwelling front. part i: Observations. *Journal of Physical Oceanography*, **50 (5)**, 1455 – 1472, https://doi.org/https://doi.org/10.1175/JPO-D-19-0203.1.

Johnson, L., C. M. Lee, E. A. D'Asaro, J. O. Wenegrat, and L. N. Thomas, 2020b: Restratification at a california current upwelling front. part ii: Dynamics. *Journal of Physical Oceanography*, **50 (5)**, 1473 – 1487, https://doi.org/https://doi.org/10.1175/JPO-D-19-0204.1.

Johnston, T. M. S., D. L. Rudnick, and E. Pallàs-Sanz, 2011: Elevated mixing at a front. *Journal of Geophysical Research: Oceans*, **116 (C11)**, https://doi.org/https://doi.org/10.1029/2011JC007192.

Lentz, S. J., 2022: Turbulent thermal-wind-driven coastal upwelling: Current observations and dynamics. *Journal of Physical Oceanography*, **52 (12)**, 2909 – 2921, https://doi.org/10.1175/JPO-D-22-0063.1.

Levy, M., R. Ferrari, P. Franks, A. Martin, and P. Riviere, 2012: Bringing physics to life at the submesoscale. *Geophys. Res. Lett.*, **39**, 1–13, https://doi.org/10.1029/2012GL052756.

Lévy, M., P. Franks, and K. Smith, 2018: The role of submesoscale currents in structuring marine ecosystems. *Nature Communications*, **9 (4758)**, https://doi.org/10.1038/s41467-018-07059-3.

McWilliams, J., 2016: Submesoscale currents in the ocean. *Proc. Roy. Soc. A*, **472**, 1–32, https://doi.org/10.1098/rspa.2016.0117.

McWilliams, J., 2017: Submesoscale surface fronts and filaments: secondary circulation, buoyancy flux, and frontogenesis. *J. Fluid Mech.*, **823**, 391 – 432, https://doi.org/10.1017/jfm.2017.294.

McWilliams, J., 2021: Oceanic frontogenesis. *Ann. Rev. Mar. Sci., in press.*, **13**, 227–53, https://doi.org/10.1146/annurev-marine-032320-120725.

McWilliams, J., J. Gula, J. Molemaker, L. Renault, and A. Shchepetkin, 2015: Filament frontogenesis by boundary layer turbulence. *J. Phys. Oceanogr.*, **45**, 1988–2005, https://doi.org/10.1175/JPO-D-14-0211.1.

Molemaker, M. J., J. C. McWilliams, and X. Capet, 2010: Balanced and unbalanced routes to dissipation in an equilibrated eady flow. *Journal of Fluid Mechanics*, **654**, 35–63, https://doi.org/10.1017/S0022112009993272.

Nagai, T., A. Tandon, and D. Rudnick, 2006: Two-dimensional ageostrophic secondary circulations at ocean fronts due to vertical mixing and large-scale deformation. *J. Geophys. Res.*, **111**, https://doi.org/10.1029/2005JC002964.

Peng, J.-P., J. Dräger-Dietel, R. P. North, and L. Umlauf, 2021: Diurnal variability of frontal dynamics, instability, and turbulence in a submesoscale upwelling filament. *Journal of Physical Oceanography*, **51 (9)**, 2825 – 2843, https://doi.org/https://doi.org/10.1175/JPO-D-21-0033.1.

Shakespeare, C., and J. Taylor, 2013: A generalized mathematical model of geostrophic adjustment and frontogenesis: uniform potential vorticity. *J. Fluid Mech.*, **736**, 366 – 413, https://doi.org/10.1017/jfm.2013.526.

Shchepetkin, A., and J. McWilliams, 2005: The Regional Oceanic Modeling System (ROMS): A split-explicit, free-surface, topography-following-coordinate ocean model. *Ocean Modell.*, **9**, 347–404, https://doi.org/10.1016/j.ocemod.2004.08.002.

Srinivasan, K., R. Barkan, and J. C. McWilliams, 2023: A forward energy flux at submesoscales driven by frontogenesis. *Journal of Physical Oceanography*, **53 (1)**, 287 – 305, https://doi.org/https://doi.org/10.1175/JPO-D-22-0001.1.

Su, Z., J. Wang, P. Klein, A. F. Thompson, and D. Menemenlis, 2018: Ocean submesoscales as a key component of the global heat budget. *Nature Communication*, **9 (775)**, https://doi.org/https://doi.org/10.1038/s41467-018-02983-w.

Sullivan, P., and J. McWilliams, 2017: Frontogenesis and frontal arrest for a dense filament in the oceanic surface boundary layer. *J. Fluid Mech.*, **837**, 341 – 380, https://doi.org/10.1017/jfm.2017.833.

Sullivan, P. P., and J. C. McWilliams, 2024: Oceanic frontal turbulence. *Journal of Physical Oceanography*, **54 (2)**, 333 – 358, https://doi.org/10.1175/JPO-D-23-0033.1.

Sun, D., and Coauthors, 2020: Diurnal cycling of submesoscale dynamics: Lagrangian implications in drifter observations and model simulations of the northern gulf of mexico. *Journal of Physical Oceanography*, **50 (6)**, 1605 – 1623, https://doi.org/10.1175/JPO-D-19-0241.1.

Swart, S., M. D. du Plessis, A. F. Thompson, L. C. Biddle, I. Giddy, T. Linders, M. Mohrmann, and S.-A. Nicholson, 2020: Submesoscale fronts in the antarctic marginal ice zone and their response to wind forcing. *Geophysical Research Letters*, **47 (6)**, e2019GL086 649, https://doi.org/https://doi.org/10.1029/2019GL086649.

Taylor, J. R., 2016: Turbulent mixing, restratification, and phytoplankton growth at a submesoscale eddy. *Geophysical Research Letters*, **43 (11)**, 5784–5792, https://doi.org/https://doi.org/10.1002/2016GL069106.

Taylor, J. R., and A. F. Thompson, 2023: Submesoscale dynamics in the upper ocean. *Annual Review of Fluid Mechanics*, **55 (1)**, 103–127, https://doi.org/10.1146/annurev-fluid-031422-095147.

Thomas, L., A. Tandon, and A. Mahadevan, 2008: Submesoscale Processes and Dynamics. *Ocean Modeling in an Eddying Regime, Geophysical Monograph Series*, **177**, 17–38, https://doi.org/10.1029/177GM04.

Thomas, L. N., J. R. Taylor, E. A. D'Asaro, C. M. Lee, J. M. Klymak, and A. Shcherbina, 2016: Symmetric instability, inertial oscillations, and turbulence at the gulf stream front. *Journal of Physical Oceanography*, **46 (1)**, 197 – 217, https://doi.org/10.1175/JPO-D-15-0008.1.

Thomas, L. N., J. R. Taylor, R. Ferrari, and T. M. Joyce, 2013: Symmetric instability in the gulf stream. *Deep Sea Research Part II: Topical Studies in Oceanography*, **91**, 96–110, https://doi.org/https://doi.org/10.1016/j.dsr2.2013.02.025.

Thompson, L., 2000: Ekman layers and two-dimensional frontogenesis in the upper ocean. *Journal of Geophysical Research: Oceans*, **105 (C3)**, 6437–6451, https://doi.org/https://doi.org/10.1029/1999JC900336.

Verma, V., H. T. Pham, and S. Sarkar, 2019: The submesoscale, the finescale and their interaction at a mixed layer front. *Ocean Modelling*, **140**, 101 400, https://doi.org/https://doi.org/10.1016/j.ocemod.2019.05.004.

Wang, T., R. Barkan, J. McWilliams, and M. J. Molemaker, 2021: Structure of submesoscale fronts of the mississippi river plume. *J. Phys. Oceanogr.*, **51**, 1113–1131, https://doi.org/10.1175/JPO-D-20-0191.1.

Wenegrat, J., and M. McPhaden, 2016: A simple analytical model of the diurnal Ekman layer. *J. Phys. Oceanogr.*, **46**, 2877–2894, https://doi.org/10.1175/JPO-D-16-0031.1n.

Wenegrat, J. O., L. N. Thomas, M. A. Sundermeyer, J. R. Taylor, E. A. D'Asaro, J. M. Klymak, R. K. Shearman, and C. M. Lee, 2020: Enhanced mixing across the gyre boundary at the gulf stream front. *Proceedings of the National Academy of Sciences*, **117 (30)**, 17 607–17 614, https://doi.org/10.1073/pnas.2005558117.

Wu, K., H. Cao, and G. Liao, 2022: Submesoscale frontal waves and instabilities driven by sheared flows. *Deep Sea Research Part II: Topical Studies in Oceanography*, **202**, 105 145, https://doi.org/https://doi.org/10.1016/j.dsr2.2022.105145.

Yang, P., Z. Jing, H. Yang, and L. Wu, 2024: A scale-aware parameterization of restratification effect of turbulent thermal wind balance. *Journal of Physical Oceanography*, https://doi.org/10.1175/JPO-D-23-0169.1.

Young, W. R., 1994: The subinertial mixed layer approximation. *Journal of Physical Oceanography*, **24 (8)**, 1812 – 1826, https://doi.org/10.1175/1520-0485(1994)024⟨1812:TSMLA⟩2.0.CO;2.

Young, W. R., and S. Jones, 1991: Shear dispersion. *Physics of Fluids A: Fluid Dynamics*, **3 (5)**, 1087–1101, https://doi.org/10.1063/1.858090.

Yu, X., A. C. Naveira Garabato, A. P. Martin, D. Gwyn Evans, and Z. Su, 2019: Wind-forced symmetric instability at a transient mid-ocean front. *Geophysical Research Letters*, **46 (20)**, 11 281–11 291, https://doi.org/https://doi.org/10.1029/2019GL084309.

Zhang, J., Z. Zhang, and B. Qiu, 2023: Parameterizing submesoscale vertical buoyancy flux by simultaneously considering baroclinic instability and strain-induced frontogenesis. *Geophysical Research Letters*, **50 (8)**, e2022GL102 292, https://doi.org/https://doi.org/10.1029/2022GL102292.

Zhang, Z., X. Zhang, B. Qiu, W. Zhao, C. Zhou, X. Huang, and J. Tian, 2021: Submesoscale currents in the subtropical upper ocean observed by long-term high-resolution mooring arrays. *Journal of Physical Oceanography*, **51 (1)**, 187 – 206, https://doi.org/10.1175/JPO-D-20-0100.1.